Computers and Concrete, *Vol.15, No.4 (2015) 515-545*
DOI: http://dx.doi.org/10.12989/cac.2015.15.4.515

Computational simulations of concrete behaviour under dynamic conditions using elasto-visco-plastic model with non-local softening

Ireneusz Marzec*, Jacek Tejchman[1] and Andrzej Winnicki[2]

[1]*Faculty of Civil and Environmental Engineering, Gdańsk University of Technology, Narutowicza Street 11/12, 80-233 Gdańsk, Poland*
[2]*Institute of Building Materials and Structures, Cracow University of Technology, Warszawska Street 24, 31-155 Cracow, Poland*

(*Received July 21, 2014, Revised October 4, 2014, Accepted November 15, 2014*)

Abstract. The paper presents results of FE simulations of the strain-rate sensitive concrete behaviour under dynamic loading at the macroscopic level. To take the loading velocity effect into account, viscosity, stress modifications and inertial effects were included into a rate-independent elasto-plastic formulation. In addition, a decrease of the material stiffness was considered for a very high loading velocity to simulate fragmentation. In order to ensure the mesh-independence and to properly reproduce strain localization in the entire range of loading velocities, a constitutive formulation was enhanced by a characteristic length of micro-structure using a non-local theory. Numerical results were compared with corresponding laboratory tests and available analytical formulae.

Keywords: concrete; characteristic length; dynamic loading; elasto-plasticity; visco-plasticity; non-local theory; strain localization; viscosity

1. Introduction

A fracture process is a fundamental phenomenon in quasi-brittle materials like concrete (Bažant and Planas 1998). It is subdivided in general into two main stages: appearance of narrow regions of intense strain localization with a certain width (including micro-cracks) and occurrence of macro-cracks (Bobiński and Tejchman 2013). Within continuum mechanics, strain localization can be numerically captured by a continuous approach and discrete macro-cracks by a discontinuous one. Usually, to describe the fracture behaviour of concrete, one approach is used. However, in order to describe the entire fracture process, a continuous approach should be connected with a discontinuous one (Simone 2003, Moonen *et al*. 2008, Bobiński and Tejchman 2013). Its description is crucial to evaluate the material strength at peak and in the post-peak regime. Fracture and strength strongly depend among others on the loading velocity since concrete is a

∗Corresponding author, Assistant Professor, E-mail: irek@pg.gda.pl
[a]Professor, E-mail: tejchmk@pg.gda.pl
[b]Professor, E-mail: andrzej@hypatia.L5.pk.edu.pl

http://www.techno-press.org/?journal=cac&subpage=8 ISSN: 1598-8198 (Print), 1598-818X (Online)

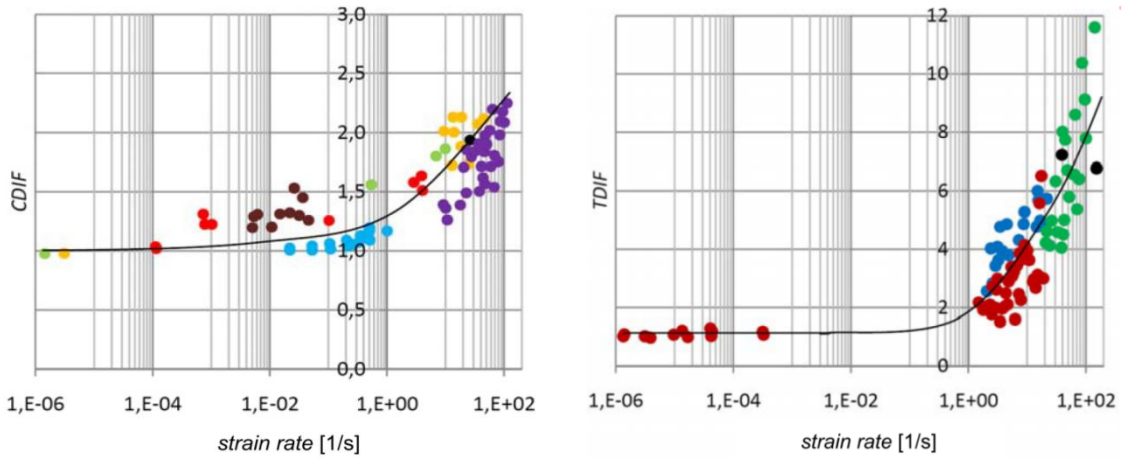

a) b)

Fig. 1 Increase of concrete strength with increasing strain rate during: a) uniaxial compression and b) uniaxial tension from different laboratory tests (CDIF – compressive dynamic increase factor, TDIF - tensile dynamic increase factor (Malvar and Ross 1998, Jankowiak 2007)

highly rate-dependent material (e.g. Winnicki *et al*. 2001, Winnicki 2007, Pedersen *et al*. 2008, Pedersen 2009, Jankowiak 2009, Jankowiak *et al*. 2011, Häußler-Combe and Kühn 2012). The structural concrete resistance increases when the strain rate increases (Bischoff and Perry 1991, 1995, Häußler-Combe and Kühn 2012) (Fig. 1) due to 3 main phenomena: 1) viscosity of moving free water in a capillary mortar system (at low strain rates), 2) inertia forces influencing the growth of micro-cracks (rate dependence of cracking) and 3) structural inertia forces (for high strain rates) (Gary 1990, Bischoff and Perry 1995, Rossi 1991, Malvar and Ross 1998, Zheng and Li 2004, Brara and Klepaczko 2006, Zhang *et al*. 2009, Ožbolt *et al*. 2011). The first two phenomena are important for low and medium strain rates, and the third one is dominant for high strain rates. The second phenomenon is strongly influenced by concrete fragmentation for high loading velocities that contributes to a significant kinetic energy dissipation (Grady 2008, Werner and Thienel 2011, Pająk 2011). The material ductility usually increases with increasing strain rate. For very high strain rates, the material behaviour after the peak can be very different (Bischoff and Perry 1995). The strength of concrete after drying is less sensitive to a loading rate. Two different phases in the strength increase with the strain rate can be distinguished in compression and tension (Fig.1). In compression, the first phase corresponds to the strain rate $\dot{\varepsilon}$ <1-10 1/s (it leads to the maximum 1.5 - time increase of the compressive strength) and the second one $\dot{\varepsilon}$ ≥1-10 1/s (it leads to the maximum 3-times increase of the compressive strength). In tension two distinct phases also occur in the tensile strength growth versus the strain rate. At $\dot{\varepsilon}$ =1 1/s the tensile strength is 2-times higher and at $\dot{\varepsilon}$ =100 1/s is even 9-times greater. The majority of the authors concluded that the strength increase in the first phase under both compression and tension was due to the presence of water in the material (in concrete pores). In turn the rate effect in compression for the second phase was considered to be of a structural origin since inertia effects in specimens under compression generated constrains similar to confining pressure which lead to the pronounced strength increase. However, the structural effect does not occur during tension.

Several theoretical papers have been published in order to describe the concrete behaviour at

global level under different prescribed strain rates by modifications of damage, plastic and elastic parts of the constitutive model (Suaris and Shah 1984, Sluys and de Borst 1992, Cervera *et al*. 1996, Nemes and Speciel 1996, Wang *et al*. 1997, Eibl and Schmidt-Hurtienne 1999, Sercombe *et al*. 2000, Denoual and Hild 2000, Gatuingt and Pijaudier-Cabot 2002, Winnicki 2007). Visco-plastic terms were usually added to model the rate effects in concrete (de Borst and Sluys 1991, Sluys and de Borst 1992, Winnicki 2007). To take into account the concrete moisture, visco-elasticity was introduced (Ragueneau and Gatuingt 2003, Pedersen *et al*. 2008). Retarded damage approaches were proposed to decrease the inertial effect in simulations since micro cracking and damage could not propagate arbitrarily fast (Häußler-Combe and Kühn 2012). In order to describe rate effects, Ožbolt and Reinhardt (2005) and Ožbolt *et al*. (2011) used a formula proposed by Bazant *et al*. (2000) within a micro-plane theory. Recently, a gradient visco-elastic retarded damage model was presented by Häußler-Combe and Kühn (2012a, 2012b) that included concrete moisture and reduced inertial effects. Bazant and Caner (2013) took into account concrete comminution into very fine particles for very high strain rates. The dynamic behaviour of concrete was also simulated at meso-level using the spherical discrete element method (DEM) (Hentz *et al*. 2004, Azevedo *et al*. 2008, Rousseau *et al*. 2009) and a continuum model enhanced by a characteristic length (Pedersen *et al*. 2008, Pedersen 2009).

The aim of our research works is to develop a reliable phenomenological constitutive model for concrete under dynamic loading for practical engineering applications. The objective of this paper was to determine the application range of an enhanced elasto-plastic continuum model with non-local softening to the concrete behaviour under dynamic conditions at macro-level (concrete composition and micro-structural phenomena at aggregate level during fracture were not taken into account). The constitutive model was enhanced either by viscosity in the plastic range or by stress modifications to capture the effect of the strain rate on the concrete behaviour. In the first case, a double length scale was present due to both non-locality and viscosity. The modelling capability of two different approaches was checked with dynamic numerical FE calculations. The dynamic calculations were carried for concrete specimens under uniaxial compression, uniaxial tension and three-point bending under the different strain rate or loading velocity. The computation results were compared with the corresponding experiments from the literature. Attention was paid to the evolution of the dynamic increase factor against the strain rate or loading velocity. In addition, a decrease of the material stiffness was considered for very high loading velocities during bending (being equivalent with material fragmentation).

The innovative points are: a) introduction of viscosity into an elasto-plastic model with non-local softening for concrete, b) a stress modification proposal for a continuum constitutive concrete model for engineering applications and c) simulations of material fragmentation for the very high loading velocity by removing finite elements. The calculations with a double length scale have not been performed yet.

2. Constitutive models for concrete under dynamic conditions

First, an elastic-visco-plastic continuum concrete model was developed based on the rate-independent elasto-plastic formulation enhanced by viscosity incorporated via the so-called overstress approach by Duvaut-Lions (1972) where the stress state was allowed to remain outside the yield surface. To describe the inviscid behaviour, the Drucker-Prager criterion (1952) in compression and the Rankine criterion (1858) in tension were assumed. In a compression regime,

a shear yield surface based on the linear Drucker-Prager criterion with isotropic hardening/softening was used (Marzec *et al*. 2007, Majewski *et al*. 2008, Tejchman and Bobiński 2013, Syroka *et al*. 2013)

$$f_1 = q + p\tan\varphi - \left(1 - \frac{1}{3}\tan\varphi\right)\sigma_c(\kappa_1), \tag{1}$$

where q – the Mises equivalent stress, p – the mean stress, φ – the friction angle, σ_c – the current uniaxial compression yield stress and κ_1 – the hardening (softening) parameter (equal to plastic strain in uniaxial compression ε_{11}^p). The internal friction angle φ was assumed as

$$\tan\varphi = \frac{3\left(1 - r_{bc}^{\sigma}\right)}{1 - 2r_{bc}^{\sigma}}, \tag{2}$$

where r_{bc}^{σ} is the ratio between the biaxial compressive strength and uniaxial compressive strength (r_{bc}^{σ}=1.2). The invariants q and p are

$$q = \sqrt{\frac{3}{2}s_{ij}s_{ji}} \qquad \text{and} \qquad p = \frac{1}{3}\sigma_{kk}, \tag{3}$$

where σ_{ij} is the stress tensor and s_{ij} denotes the deviatoric stress tensor. The flow potential was defined as

$$g_1 = q + p\tan\psi, \tag{4}$$

where ψ is the dilatancy angle ($\psi \neq \varphi$). For the sake of simplicity, the constant values of ψ and φ were assumed. In turn, in a tensile regime, the maximum tensile stress criterion by Rankine (1858) was used with a yield function f_2 and isotropic softening defined as (Marzec *et al*. 2007, Majewski *et al*. 2008, Tejchman and Bobiński 2013, Syroka *et al*. 2013)

$$f_2 = \max\{\sigma_1, \sigma_2, \sigma_3\} - \sigma_t(\kappa_2), \tag{5}$$

where σ_i – the principal stress, $\sigma_t(\kappa_2)$ – the tensile yield stress and κ_2 – the softening parameter equal to the maximum principal plastic strain ε_1^p. The associated flow rule was assumed. The edges and vertex in Rankine yield function were taken into account by applying a standard multi-surface plasticity model with the Koiter's rule in order to calculate plastic strain increments. The same procedure was adopted in the case of combined tension (Rankine criterion) and compression (Drucker-Prager criterion) (there are sharp edges along the lines where the surface in Eq. (1) intersects the Rankine planes). This inviscid isotropic elasto-plastic model for concrete (Eqs. (1)-(5)) requires two elastic parameters: modulus of elasticity E and Poisson's ratio υ, one compression stress function $\sigma_c = f(\kappa_1)$ (based on a uniaxial compression test), one tensile stress function $\sigma_t = f(\kappa_2)$ (based on a uniaxial tension test), internal friction angle φ and dilatancy angle ψ (based on a triaxial compression test). The model has some shortcomings. The shape of the failure surface in the p-q plane is linear (not parabolic as in the reality). The

tensile and compression meridians are straight and the shape of the yield curve in a deviatoric plane is circular for compression and triangular for tension. Thus it does not gradually change from a curvilinear triangle with smoothly rounded corners to nearly circular with increasing pressure (as in the reality). The strength is the same for a triaxial compression and extension test (it does not depend on the Lode angle) and the stiffness degradation due to strain localization and non-linear volume changes during loading are not taken into account. These disadvantages may be overcome by adopting more advanced constitutive laws (e.g. by Menetrey and Willam (1995) and by Lee and Fenves (1998)).

The viscosity was incorporated based on the approach by Duvaut-Lions (1972), wherein a viscoplastic solution was simply constructed based on a relevant plastic solution. The advantage of this approach is the easy numerical implementation since an additional simple stress update loop is needed in existing elasto-plastic algorithms only. The visco-plastic strain rate and hardening parameter were respectively defined as

$$\dot{\varepsilon}_{ij}^{vp} = \frac{1}{\tau}\left[C_{ijkl}^{e}\right]^{-1}\left(\sigma_{kl} - \bar{\sigma}_{kl}\right) \tag{6}$$

and

$$\dot{\kappa}^{vp} = \frac{1}{\tau}\left(\kappa - \bar{\kappa}\right), \tag{7}$$

where τ is the material parameter usually called the relaxation time, $\bar{\sigma}_{ij}$ and $\bar{\kappa}$ are the stress and hardening/softening parameter of the inviscid material and C_{ijkl}^{e} is the linear elastic stiffness tensor with the Young modulus E and Poisson ratio υ. The visco-plastic strain rate Eq. (6) was defined by the difference between the true stresses and stresses obtained in an inviscid material. The total strain rate partition into an elastic strain rate and a visco-plastic strain rate was assumed

$$\dot{\varepsilon}_{ij} = \dot{\varepsilon}_{ij}^{e} + \dot{\varepsilon}_{ij}^{vp}. \tag{8}$$

Such a formulation allows for a smooth transition from an inviscid to a viscous case (in contrast to the visco-plastic model by Perzyna (1966)). The Duvaut-Lions model can be combined with a yield surface which has an apex or a non-smooth surface which is not possible with the model by Perzyna requiring a smooth surface with continuous derivatives with respect to the stress in order to determine the unique direction of a visco-plastic strain rate. The material is initially considered to be as a rate-independent, so the plastic stress tensor $\bar{\sigma}_{ij}$ and the hardening variable $\bar{\kappa}$ are obtained. Later, the rate-dependency is incorporated by means of Eqs. (6) and (7). Finally, one obtains the updated visco-plastic stress and updated visco-plastic hardening parameter integrated over the time step Δt (from 't' up to '$t+\Delta t$')

$$\sigma_{ij}^{n+1} = \frac{\left(\sigma_{ij}^{n} + C_{ijkl}^{e} : \Delta\varepsilon_{kl}\right) + \dfrac{\Delta t}{\tau}\bar{\sigma}_{ij}^{n+1}}{1 + \dfrac{\Delta t}{\tau}}, \tag{9}$$

$$\kappa_{n+1} = \frac{\kappa_n + \dfrac{\Delta t}{\tau}\bar{\kappa}_{n+1}}{1+\dfrac{\Delta t}{\tau}}. \tag{10}$$

A Duvaut-Lions visco-plastic model is quite convenient to be implemented, since a visco-plastic solution is the update of an inviscid one (Winnicki 2007). It introduces a characteristic length into the field equations as a multiplication product of the elastic wave speed times the relaxation time (de Borst and Sluys 1991).

In addition, as a separate model, the effect of the strain rate was included into our elasto-plastic constitutive model with non-local softening by means of the so-called activation energy theory (called also the dynamic plasticity) proposed by Bažant *et al*. (2000)

$$\sigma_{ij}^{d} = \sigma_{ij}^{0}\left[1 + C_2 \ln\left(\frac{2\dot{\gamma}}{C_1}\right)\right] \quad \text{with} \quad \dot{\gamma} = \sqrt{0.5\dot{\varepsilon}_{ij}\dot{\varepsilon}_{ij}}\,, \tag{11}$$

where σ_{ij}^{d} is the dynamic stress tensor, σ_{ij}^{0} denotes the static stress tensor, $\dot{\varepsilon}_{ij}$ is the strain rate tensor, $\dot{\gamma}$ - the second strain rate invariant and C_1 and C_2 - the empirical material constants. Analogously, we proposed a more complex non-linear formulation, composed of 3 functions versus $\dot{\gamma}$

$$\sigma_{ij}^{d} = \begin{cases} \sigma_{ij}^{0}\left[\omega(\boldsymbol{\sigma})\left(\dfrac{\dot{\gamma}}{\dot{\varepsilon}_s}\right)^{C_1} + \left(1-\omega(\boldsymbol{\sigma})\right)\left(\dfrac{\dot{\gamma}}{\dot{\varepsilon}_s}\right)^{C_2}\right] & \text{at} \quad \dot{\gamma} \le 40 \text{ 1/s} \\ \sigma_{ij}^{0}\left[\omega(\boldsymbol{\sigma})\left(\dfrac{\dot{\gamma}}{\dot{\varepsilon}_s}\right)^{C_1} + \left(1-\omega(\boldsymbol{\sigma})\right)\left(\dfrac{\dot{\gamma}}{\dot{\varepsilon}_s}\right)^{C_4}\right] & \text{at} \quad 401\text{/s} < \dot{\gamma} \le 100 \text{ 1/s}, \\ \sigma_{ij}^{0}\left[\omega(\boldsymbol{\sigma})\left(\dfrac{\dot{\gamma}}{\dot{\varepsilon}_s}\right)^{C_3} + \left(1-\omega(\boldsymbol{\sigma})\right)\left(\dfrac{\dot{\gamma}}{\dot{\varepsilon}_s}\right)^{C_2}\right] & \text{at} \quad \dot{\gamma} > 100 \text{ 1/s} \end{cases} \tag{12}$$

where $\dot{\varepsilon}_s$ - the reference strain rate equal to 1×10^{-5}, C_1-C_4 – the empirical material constants and $\omega(\boldsymbol{\sigma})$ - the stress weight function which is determined with aid of principal stresses (Lee and Fenves 1998)

$$\omega(\boldsymbol{\sigma}) = \begin{cases} 0 & \text{if} \quad \boldsymbol{\sigma} = 0 \\ \dfrac{\sum\langle\sigma_{\mathrm{i}}\rangle}{\sum|\sigma_{\mathrm{i}}|} & \text{otherwise} \end{cases}, \tag{13}$$

where the Macauley bracket is defined by the formula $\langle x\rangle = \frac{1}{2}\left(|x| + x\right)$. The stress weight function can be treated as a positive-negative stress projection operator which allows for a simple differentiation between tension and compression (e.g. under pure tension the stress weight function is $w = 1$ and under pure compression $w = 0$).

As compared to Eq. (11), the rate effect in concrete in Eq. (12) was divided into 3 ranges of $\dot{\gamma}$

with 2 different phases of the strength growth (first phase with a moderate growth and second phase with a rapid one) in order to obtain a better agreement with the experimental results (Fig. 1). In addition, the strength growth rate was assumed to be stronger under tension than under compression (as in experiments). The inviscid elasto-plastic stress tensor ($\bar{\sigma}_{ij}$) obtained with Eqs. (1)-(5) was updated according to Eqs. (11) and (12) by assuming that $\sigma_{ij}^{0} = \bar{\sigma}_{ij}$.

3. Modelling of strain localization

An integral-type non-local theory was used as a regularization technique to describe strain localization in the entire strain rate range (Pijaudier-Cabot and Bažant 1987, Brinkgreve 1994, Vermeer and Brinkgreve 1994, Ferrara and di Prisco 2001, Bažant and Jirásek 2002, Pijaudier-Cabot *et al*. 2004). It takes advantage of a weighted spatial averaging of a suitable state variable over a neighbourhood of each material point. Thus, a state variable at a certain material point depends not only on the state variable at the point but on the distribution of the state variable in a finite neighbourhood of the point considered (the principle of a local action does not hold – a non-local interaction takes place between any two points). It has a physical motivation in the fact that the distribution of stresses in the interior of concrete at meso-scale is strongly non-uniform due to the presence of different phases (aggregate, cement matrix, transitional interfacial zones). Polizzotto *et al*. (1998) laid down a thermodynamically consistent formulation of non-local plasticity. Usually, in elasto-plastic formulations, it is sufficient for achieving mesh-independent FE results to treat non-locally one state variable controlling material softening (e.g. non-local softening parameter), whereas stresses, strains and other variables remain local (Brinkgreve 1994, Vermeer and Brinkgreve 1994, Jirásek and Rolshoven 2006, Bobiński and Tejchman 2004).

In the case of dynamic problems, the viscosity provides an appropriate solution for regularization of initial value problems (de Borst and Sluys 1991). However, in order to properly regularize quasi-static FE analysis results, the viscous parameter has to be unrealistically high. Therefore, the non-locality was introduced into the constitutive formulation in an inviscid phase of the model for the entire loading range (although its presence for very high strain rates is questionable due to the material fragmentation). The rates of the inviscid softening parameter Eq. (7) were averaged according to Brinkgreve (1994) and Vermeer and Brinkgreve (1994)

$$\mathrm{d}\tilde{\bar{\kappa}}_i(\boldsymbol{x}) = \mathrm{d}\bar{\kappa}_i(\boldsymbol{x}) + m\left(\int_V \bar{\omega}(\boldsymbol{x},\xi)\mathrm{d}\bar{\kappa}_i(\xi)\mathrm{d}\xi - \mathrm{d}\bar{\kappa}_i(\boldsymbol{x})\right), \tag{14}$$

where $\mathrm{d}\tilde{\bar{\kappa}}_i$ detones the non-local softening parameter and and V is the material volume. Since the rate of the softening parameter is not known at the iteration beginning, some extra sub-iterations are required to solve Eq. (14) (Strömberg and Ristinmaa 1996). To simplify the calculations, the non-local rates were replaced by their approximations $\mathrm{d}\bar{\kappa}_i^{est}$ calculated based on the known total strain rate (Brinkgreve 1994, Vermeer and Brinkgreve 1994)

$$\mathrm{d}\tilde{\bar{\kappa}}_i(\boldsymbol{x}) \approx \mathrm{d}\bar{\kappa}_i(\boldsymbol{x}) + m\left(\int_V \bar{\omega}(\boldsymbol{x},\xi)\mathrm{d}\bar{\kappa}_i^{est}(\xi)\mathrm{d}\xi - \mathrm{d}\bar{\kappa}_i^{est}(\boldsymbol{x})\right), \tag{15}$$

where in $\bar{\omega}$ is the weighting function (called also the attenuation function or non-local averaging function). The FE results have shown an insignificant influence of the calculation method of the

rates of the non-local softening parameter (Bobiński and Tejchman 2004). In addition, an approximate method proposed by Brinkgreve (1994) and Vermeer and Brinkgreve (1994) in Eq. (15) is less time consuming (by ca.30%).

As the weighting function $\overline{\omega}$, the Gauss distribution was assumed (Bažant and Jirásek 2002) independently of strain rates

$$\overline{\omega}(r)=\frac{1}{c_g}e^{-\left(\frac{r}{l_c}\right)^2}, \tag{16}$$

where the parameter l_c is the characteristic length of micro-structure related to a micro-structural dimension as e.g. the maximum aggregate size in concrete (Bažant and Planas (1998), r is the distance between two material points and c_g denotes the normalizing factor equal to $\sqrt{\pi}l_c$ (1D case), πl_c^2 (2D case) and $\pi\sqrt{\pi}l_c^3$ (3D case). The averaging in Eq. (15) is restricted to a small representative area around each material point (the influence of points at the distance of $r=3\times l_c$ is only of 0.01%). The weighting function satisfies the normalizing condition (Pijaudier-Cabot and Bažant 1987)

$$\overline{\omega}(r,\zeta)=\frac{\omega_0(\|x-\zeta\|)}{\int_V \omega_0(\|x-\zeta\|)\mathrm{d}\zeta}. \tag{17}$$

The characteristic length l_c is about 5 mm in usual concretes based both on our numerical simulation results of both concrete and reinforced concrete beams under bending when using the Gauss distribution function and experiments using a digital image correlation DIC technique for measuring the width of a localized zone on the concrete surface (Skarżyński and Tejchman 2010, Skarżyński *et al*. 2011, Syroka-Korol and Tejchman 2013). A proper non-local transformation requires that a non-local field corresponding to a constant local field remains constant in the vicinity of a boundary.

The models where implemented into the ABAQUS STANDARD program (2004) with the aid of the subroutine UMAT (user constitutive law definition) and UEL (user element definition). For the solution of a non-linear equation of motion governing the dynamic response of a system of finite elements, the Newmark algorithm was used. The calculations were performed with a symmetric elastic global stiffness matrix instead of applying a tangent stiffness matrix (the choice was governed by access limitations to the commercial software ABAQUS (2004)). The procedure yielded sufficiently accurate and fast convergence. The following convergence criteria were assumed

$$r_{\max}\le 0.01\tilde{q} \quad \text{and} \quad c_{\max}\le 0.01\Delta u_{\max}, \tag{18}$$

where $r_{\max}$ - the largest residual out-of-balance force, $\tilde{q}$ - the average value of all elements and externally applied forces in the model (so-called the spatial average force), $c_{\max}$ – the largest correction of the displacement and $\Delta u_{\max}$ – the largest change of the displacements in the increment. The time increment was $\Delta t = t/600$ - $t/6000$ with $t = 10^{-5}$-10^{3} s - the total calculation time. To satisfy the consistency condition df=0 in elasto-plasticity, a linearized expansion of the

yield condition about the trial stress point using an elastic predictor and a plastic corrector with the return mapping algorithm (Ortiz and Simo 1986) was applied. The calculations were always carried out using a large-displacement analysis although the effect of large displacements turned out to be negligible. In this case, the current configuration of the body was considered. The Cauchy stress was taken as the stress measure. The conjugate strain rate was the rate of deformation. The rotation of the stress and strain tensor was calculated with the Hughes-Winget method (1980)

$$\sigma_{ij}^{t+\Delta t} = \Delta R_{ik} \Delta R_{jl} \sigma_{kl}^{t} + \Delta \breve{\sigma}_{ij} , \tag{19}$$

where $\Delta \breve{\sigma}_{ij}$ is the stress increment caused by the straining of the material during this time increment. The increment in rotation ΔR_{ij} is define as

$$\Delta R_{ij} = \left(I_{ik} - \frac{1}{2} \Delta W_{ik} \right)^{-1} \left(I_{kj} - \frac{1}{2} \Delta W_{kj} \right), \tag{20}$$

where ΔW_{ij} is the central difference integration of the spin rate. As a consequence of the assumption of the geometrical nonlinearity, a non-local averaging was performed in the current configuration. This choice was also governed by the fact that element areas in this configuration were automatically calculated by ABAQUS.

The local elasto-visco-plastic model requires four material constants to capture the elastic and plastic behaviour: E, ν, φ and ψ and two hardening/softening yield stress functions (one in tension and one in compression) which have a major impact on the results. The constants and yield stress functions can be determined for concrete with the aid of two independent simple monotonic tests: uniaxial compression test and uniaxial tension (or three-point bending) test. In addition, one material constant τ is required to describe the viscous behaviour that requires several tests during uniaxial compression and uniaxial tension to capture the strength increase factor for various strain rates.

4. Dynamic FE results

4.1 Uniaxial compression

The standard concrete cube (150×150×150 mm^3) was numerically modelled either in a plane strain or 3D state. It was completely fixed at the lower edge and fixed in a horizontal direction along the upper edge. The uniform vertical displacement was imposed in the range of Δ=0-1.0 mm at the upper boundary to induce deformation (Fig. 2). The material parameters were: E=35.0 GPa, ν=0.15, φ=14°, ψ=8° and the compressive ultimate stress σ_c=30 MPa with linear softening (H = 1.55 GPa). The imposed vertical strain rate at the top edge was varied from $\dot{\varepsilon}$=10^{-5} 1/s up to $\dot{\varepsilon}$=10^{2} 1/s. The different meshes were assumed: 10×10×10 and 15×15×15 with eight-node brick elements and full integration (3D analyses) and 10×10, 20×20 and 40×40 consisting of plane strain triangular elements in the so-called "union jack pattern" and plane strain four-node square elements with full integration (2D analyses) (Fig. 2). In order to prevent the element locking in the

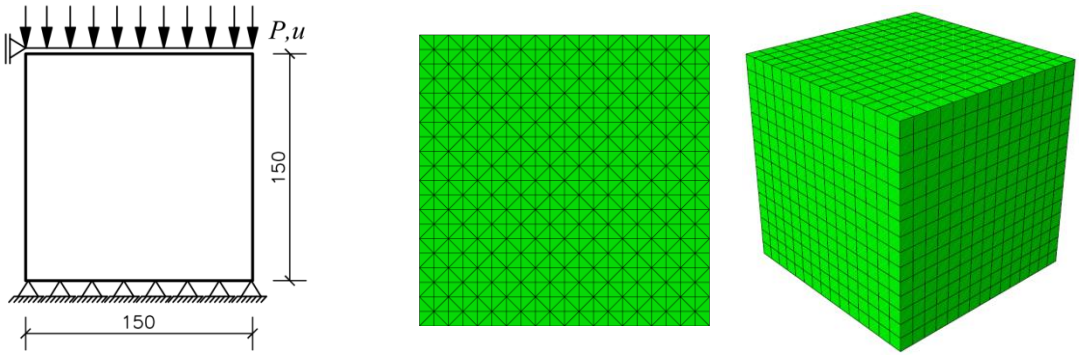

a) b)

Fig. 2 Uniaxial compression test in FE calculations: a) specimen geometry with boundary conditions and b) mesh discretization (2D analyses - plane strain triangular elements, 3D analyses - eight-node brick elements)

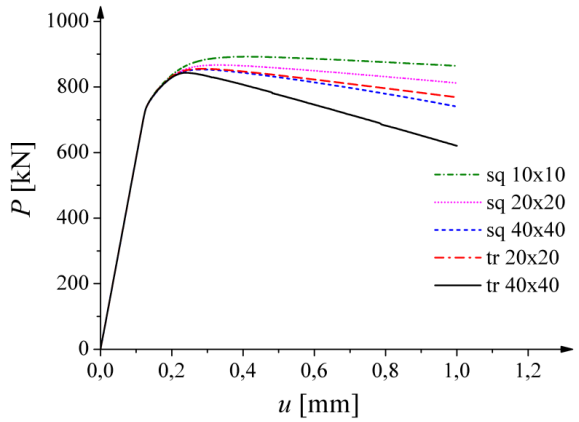

a)

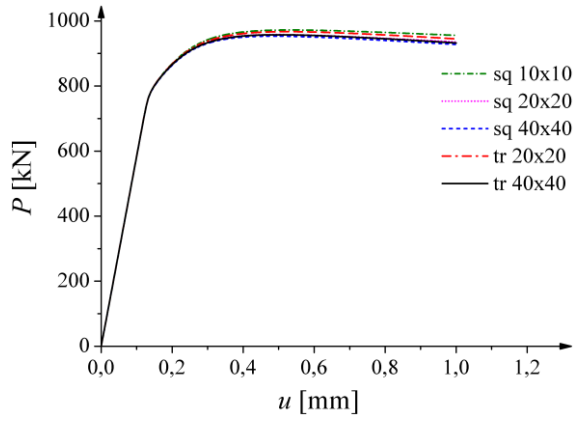

b)

Fig. 3 The calculated force-displacement curves using elasto-visco-plastic model (τ=2×10^{-6} s) with local softening for different 2D mesh densities: a) during slow loading process ($\dot{\varepsilon}$ =10^{-4} 1/s) and b) during fast loading process ($\dot{\varepsilon}$ =1 1/s)

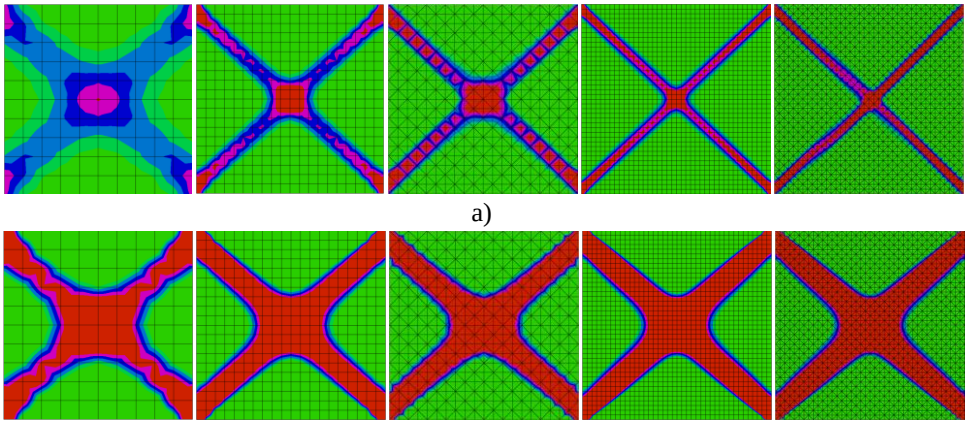

a)

b)

Fig. 4 The calculated contours of softening parameter using elasto-visco-plastic model ($\tau=2\times10^{-6}$ s) with local softening for different 2D mesh densities: a) during slow loading process ($\dot{\varepsilon}=10^{-4}$ 1/s) and b) during fast loading process ($\dot{\varepsilon}=1$ 1/s)

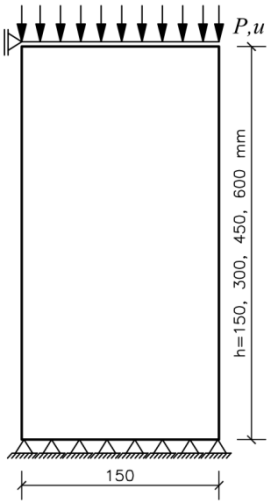

Fig. 5 The geometry and boundary conditions for 2D specimens with different height under uniaxial compression in FE calculations of size effect (width b =150 mm)

case of the full integration, the actual volume changes at the Gauss points were replaced by the average volume change of the element (it is so-called a selectively reduced-integration technique, Nagtegaal *et al*. 1977). The element size changed between 3.75 mm (fine mesh) and 15 mm (coarse mesh). The relaxation time τ was equal to 1×10^{-6} s, 2×10^{-6} s, 1×10^{-5} s, 2×10^{-5} s and 2×10^{-4} s. The characteristic length, $l_c=2\tau\times c_e$ (de Borst and Sluys 1991), where c_e=3800 m/s denotes the longitudinal wave velocity for the assumed density of 2400 kg/m^3, could theoretically vary in the range of 7.6-1520 mm. In the computations, the characteristic length had the value of 5-15 mm.

Initially, plane strain quasi-static calculations within the elastic-visco-plastic model with local softening (softening modulus H=0.3 GPa) were carried out. The calculations were performed without inertial forces during the so-called slow process (the prescribed vertical normal strain rate

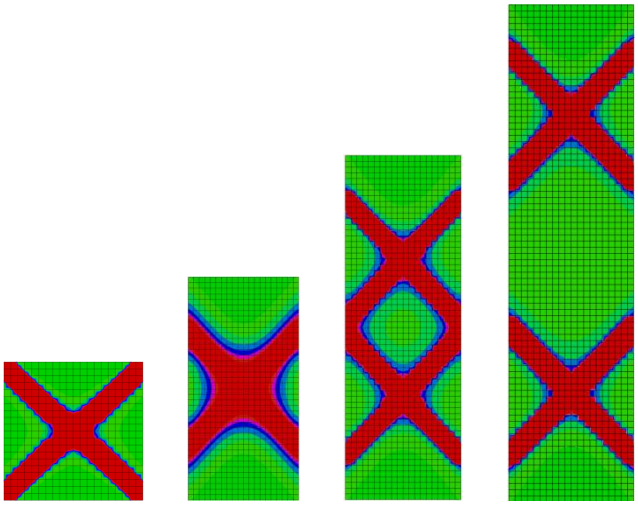

a) b) c) d)

Fig. 6 The calculated contours of softening parameter with elasto-visco-plastic model and local softening during fast loading without inertial forces ($\dot{\varepsilon}$ =1 1/s, τ=2×10^{-5} s) for different 2D specimen heights: a) h=150 mm, b) h=300 mm, c) h=450 mm and d) h=600 mm for top vertical normal strain of ε =0.01 (specimen width b=150 mm)

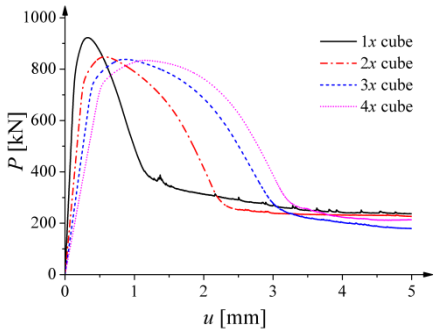

a)

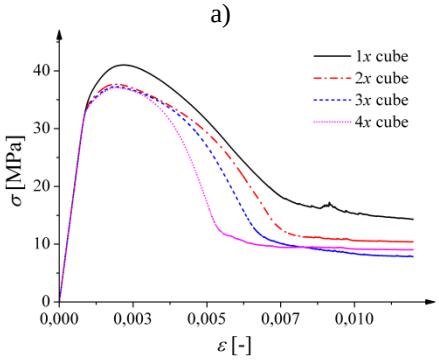

b)

Fig. 7 The calculated force-displacement P-u (a) and stress-strain σ-ε (b) curves with elasto-visco-plastic model and local softening during fast loading for different 2D specimen heights from quasi-static calculations ($\dot{\varepsilon}$ =1 1/s, τ=2×10^{-5}, b =150 mm)

A)

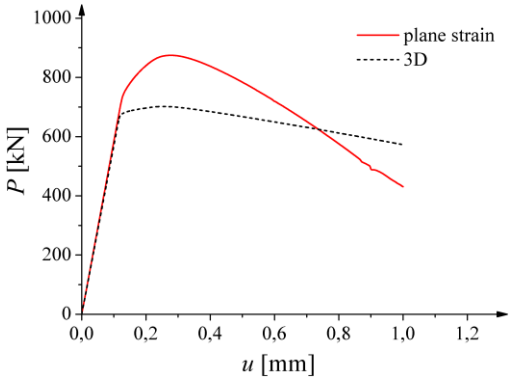

B)

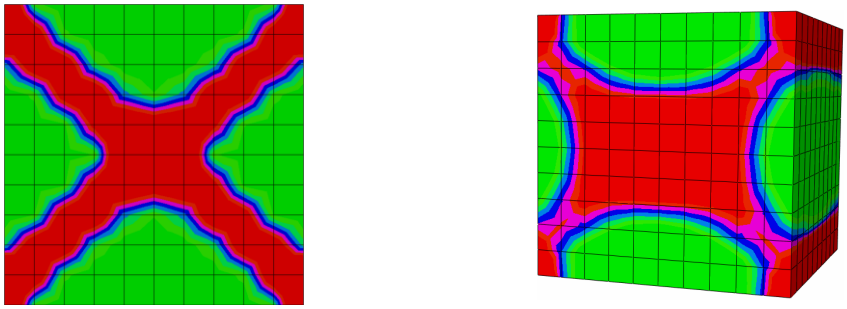

a) b)

Fig. 8 Uniaxial compression with elasto-visco-plastic model with local softening (fast loading process ($\dot{\varepsilon}$ =1 1/s, τ=2×10^{-6} s) under 2D plane strain (a) and 3D deformation (b): A) force-displacement curves and B) contours of softening parameter

A)

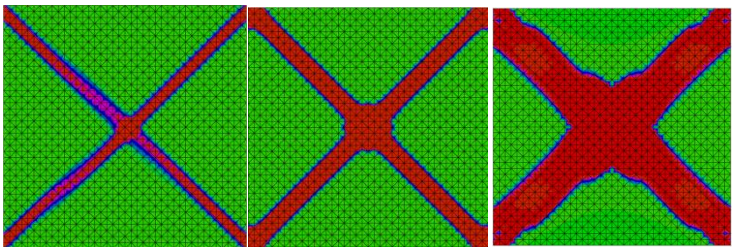

a) b) c)

B)

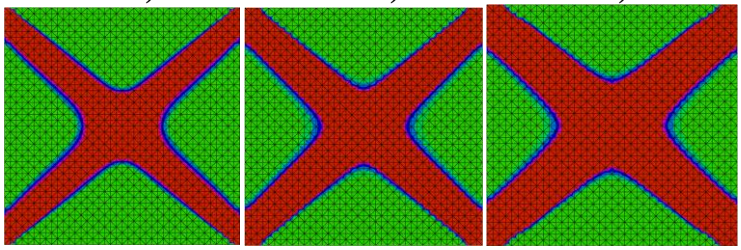

a) b) c)

Fig. 9 The contours of softening parameter for slow (A) and fast (B) loading in 2D simulations: a) elasto-visco-plastic model with local softening (l_c=0 mm), b) elasto-visco-plastic model with non-local softening (l_c=5 mm), c) elasto-visco-plastic model with non-local softening (l_c=15 mm)

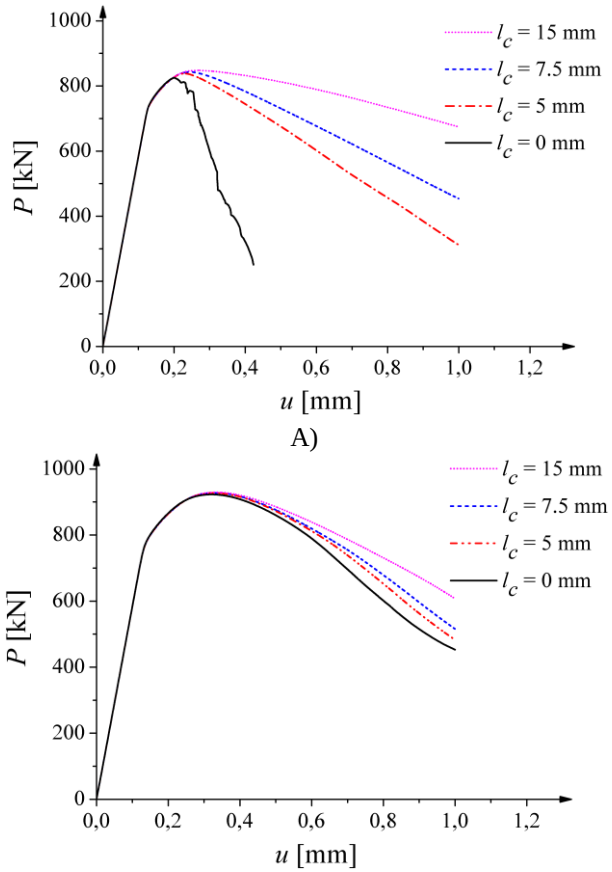

Fig. 10 Calculated force-displacement curves with elasto-visco-plastic model with local and non-local softening (at τ=2×10^{-6} s) for different characteristic lengths of microstructure l_c in 2D simulations: A) slow loading ($\dot{\varepsilon}$ =10^{-4} 1/s), B) fast loading ($\dot{\varepsilon}$ =1 1/s)

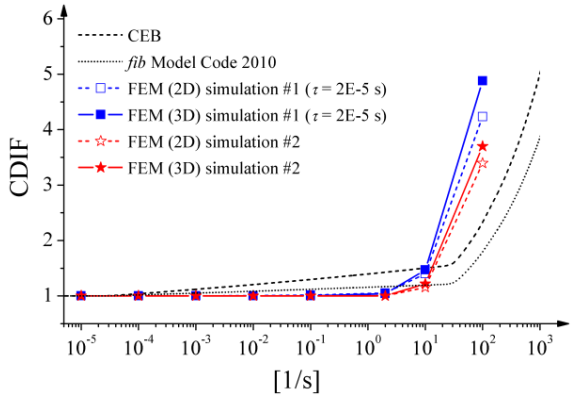

Fig. 11 Dynamic FE simulations showing effect of formulation and viscosity based on evolution of dynamic compressive increase factor CDIF by CEB and *fib* Model Code: #1 - elasto-visco-plastic model with non-local softening (l_c=5 mm) and τ=2×10^{-5} s, #2 - elasto-plastic model with non-local softening (l_c=5 mm)

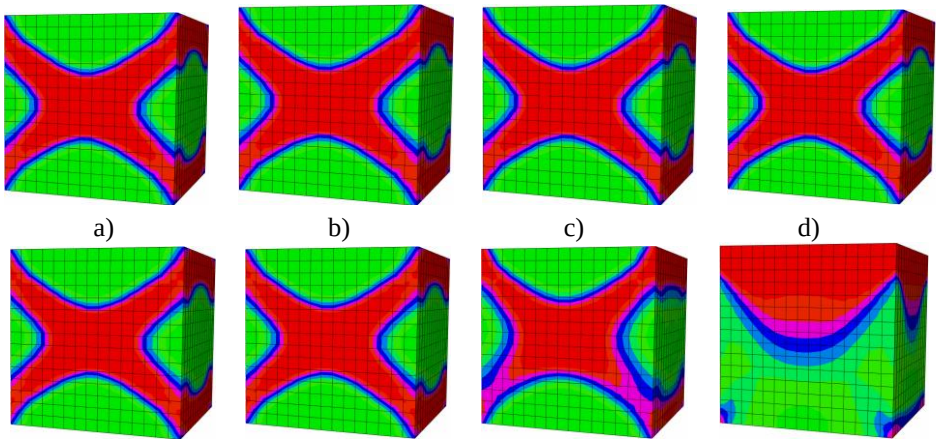

Fig. 12 The contours of non-local softening parameter from 3D FE dynamic simulations for different prescribed strain rates: a) 10^{-5} 1/s, b) 10^{-4} 1/s, c) 10^{-3} 1/s, d) 10^{-2} 1/s, e) 10^{-1} 1/s, f) 10^{0} 1/s, g) 10^{1} 1/s, h) 10^{2} 1/s using elasto-visco-plastic model with non-local softening (τ=1×10^{-6} s, l_c=5 mm)

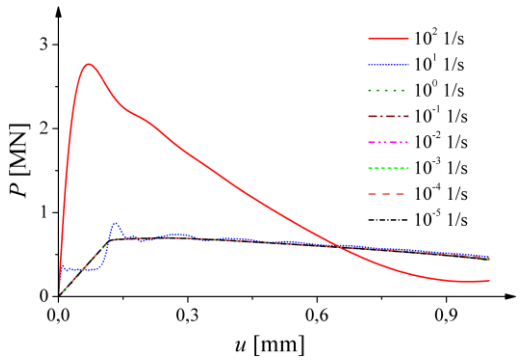

Fig. 13 The load-displacement curves from FE analyses for different vertical strain rate using elasto-visco-plastic model with non-local softening in 3D simulations (τ=1×10^{-6} s, l_c=5 mm)

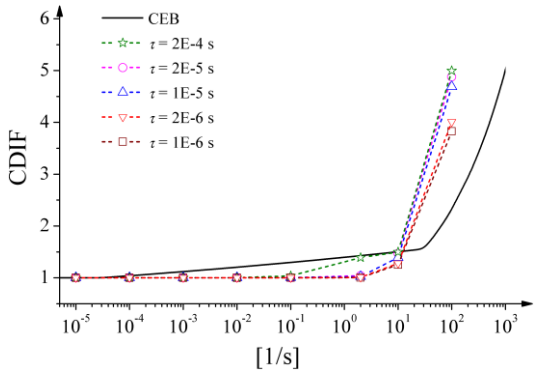

Fig. 14 Dynamic 3D FE results of CDIF using elasto-visco-plastic model with non-local softening (l_c = 5 mm) with different relaxation times τ as compared to CEB curve

along the top edge was $\dot{\varepsilon}=10^{-4}$ 1/s) and the fast process ($\dot{\varepsilon}=1$ 1/s) (Figs. 3 and 4). The viscosity parameter was $\tau = 2\times10^{-6}$ s. The third dimension was taken as 0.15 m.

The FE results of Figs. 3(a) and 4(a) are evidently mesh-dependent during the slow process since the crossing shear zones are confined to one or two rows of finite elements only. For each mesh, a mesh-dependent post-peak response was obtained. Thus, the viscous terms are not sufficient to properly regularize the boundary value problem. In turn, for the fast process, the mesh-dependence does not occur (Figs. 3(b) and 4(b)) and shear zones have larger widths than one element row.

For all meshes the width of the localization zone is very similar and approximately equal to 22 mm (Fig. 4(b)). The calculated both geometry of localized zones and load-displacement curves are similar as in FE calculations by Winnicki (2007).

In order to determine the effect of the specimen height during the fast compressive loading ($\dot{\varepsilon}=1$ 1/s), the 2D plane strain FE quasi-static calculations using four-node square elements with full integration were performed with the constant specimen width of b=150 mm and varying specimen height between 150 mm and 600 mm (with $\tau=2\times10^{-5}$ s and b=150 mm) (Fig. 5).

For lower specimens (h=150-300 mm), two intersecting shear zones are obtained (Fig. 6). In turn, for h=450-600 mm four shear zones occur. At ε = 1%, the width of the calculated shear zones is 29 mm (h=150 mm), 36 mm (h=300 mm) and 35 mm (h=450-600 mm). The material brittleness increases with increasing height (Fig. 7). The highest maximum vertical normal stress is for h=150 mm. For the heights in the range of h=300-600 mm, the maximum stress is almost the same that indicates a weak size effect during compression.

Fig. 8 shows the effect of the assumed modelling (plane strain or 3D state) for fast loading during compression. The computations were performed with the parameters: H=1.0 GPa and $\tau=2\times10^{-6}$ s. In the case of 3D the same boundary condition as in 2D were assumed. The calculated strength under plane strain conditions was higher as compared with the 3D strength by 25% due to the large compressive stress in the lateral direction. The shape of localized zones was similar. In the narrowest place, the width of the shear zone was approximately 26 mm for 2D and 24 mm for 3D. In the central specimen part, the shape of a 3D localized zone was more diffuse and had a significantly larger width. The 3D calculations are certainly more realistic due to the ability to properly simulate inertia effects which generate strong constraints.

The non-locality effect on 2D FE quasi-static results using the elasto-visco-plastic model is demonstrated in Figs. 9 and 10 (for $\tau=2\times10^{-6}$ s, H=1.55 GPa). Due to presence of a characteristic length of micro-structure (l_c=5-15 mm) in an inviscid phase (the phase in which the viscous terms are not active), shear zones are also mesh-independent for a slow loading process (Fig. 9A). The width of a localized zone increases obviously with increasing l_c (Fig. 9A): 6.7 mm (l_c=0 mm), 13.5 mm (l_c=5 mm), 24 mm (l_c=15 mm). The width of the shear zones for the high strain rate is: 22 mm (l_c=0 mm), 25 mm (l_c=5 mm) and 31 mm (l_c=15 mm) and the edges of shear zones become smoother (Fig. 9B). The width of the shear zones increases also with increasing strain rate (Figs. 9Ab and 9Bb) for the same value of l_c. For fast loading, the overlapping effect of both the non-locality and viscosity occurs – the shear zone width increases by 10-45% (from 22 mm up to 31 mm, Figs. 9Ba-9Bc). With increasing l_c, the material ductility increases in particular during slow loading (Fig. 10).

Next, the effect of several different prescribed strain rates ranging from 10^{-5} 1/s up to 100 1/s on the concrete dynamic behaviour was investigated (including inertia effects into FE computations). The numerical strength was compared with the compressive dynamic increase factor (CDIF) according to the CEB-FIP Model Code 1990 (1993). It should be mentioned that in

the newest version of *fib* Model Code 2010 (2012) (*fib* being a successor of CEB), some smaller values of CDIF and TDIF were introduced (Fig. 11).

In the first step, the dynamic FE results using the elasto-visco-plastic model (simulation #1, $\tau = 2\times10^{-5}$ s) and the elasto-plastic model (simulation #2) with non-local softening ($l_c = 5$ mm) were compared during 2D and 3D calculations (Fig. 11). The calculated dynamic increase factor is underestimated as compared to CEB or *fib* Model Code 2010 for the strain rates $\dot{\varepsilon} \leq 1$ 1/s. In turn, for the high strain rates ($\dot{\varepsilon} > 10$ 1/s), the calculated dynamic increase factor is always overestimated since fragmentation is not taken into account. The increase of CDIF is more pronounced in 3D simulations than in simplified 2D analyses. In the case of viscous simulations, CDIF obviously increases faster than in non-viscous studies for $\dot{\varepsilon} \geq 1$ 1/s (Fig. 11). The calculation differences are lager when comparing our FE results to CEB than to *fib* Model Code 2010.

The shape and width (about 30 mm) of shear zones and load-displacement curves are practically the same for strain rates $\dot{\varepsilon} \leq 1$ 1/s (Figs. 12 and 13). For $\dot{\varepsilon} = 100$ 1/s (when using elasto-visco-plastic model with non-local softening), instead of intersecting shear zones, a localized region occurs at the top edge and the material indicates a stiffer response in an elastic domain and more brittle one in a softening regime (Fig. 12(h)). Fig. 13 shows a significant influence of inertia effects on the shape of the load-displacement curve for the high strain rates $\dot{\varepsilon} \geq 10^1$ 1/s in the elasto-visco-plastic simulation).

The influence of the relaxation time τ in the range $\tau = 1\times10^{-6}$–2×10^{-4} s is shown in Fig. 14 using the 3D elasto-visco-plastic model with non-local softening. An increase of the viscosity parameter leads to a faster strength growth, however for the high strain rates ($\dot{\varepsilon} \geq 10^1$ 1/s) only. For the highest strain rates, CDIF is significantly overestimated. Thus, concerning concrete elements loaded in compression, viscosity in a plastic domain has some effect only for high strain rates ($\dot{\varepsilon} \geq 10^1$ 1/s).

Finally, the 3D results of numerical simulations with the elasto-plastic model with non-local softening and the stress modification by Eqs. (11) and (12) are shown in Figs. 15 and 16. One simulation was carried out with the elasto-plastic model (simulation #1), one with the elasto-visco-plastic model with $\tau = 1\times10^{-6}$ s (simulation #2) and two simulations with the elasto-plastic model with the stress modifications: the simulation #3a with the parameters $C_1 = 1\times10^{-6}$ and $C_2 = 80\times10^{-4}$ using Eq. (11) and the simulation #3b with the parameters $\dot{\varepsilon}_s = 1\times10^{-5}$, $C_1 = 0.05$, $C_2 = 0.02$, $C_3 = 0.07$ and $C_4 = -0.002$ using Eq. (12). A clear improvement of the calculated curve CDIF as compared to the previous results was obtained in the simulation #3b when using the elasto-plastic model with our stress modification given by Eq. (12).

The calculated curve shape is similar to the experimental one. For the high strain rates, the calculated CDIF was again overestimated but to a smaller grade. Similarly as before the shape and width (about 24 mm) of the shear zones are practically the same for the strain rates $\dot{\varepsilon} \leq 1$ 1/s (Fig. 16). For the strain rate $\dot{\varepsilon} = 10^1$ 1/s, the shape of shear localization starts to change and its width increases (up to 34 mm). Finally for $\dot{\varepsilon} = 100$ 1/s, instead of intersecting shear zones, a localized region occurs at the top edge.

4.2 Uniaxial tension test

A dumbbell-shaped specimen subjected to uniaxial tension was modelled as in the experiments by Yan and Lin (2006) (Fig. 17). The following material parameters were assumed in FE

calculations: E=29.0 GPa, ν=0.20, the initial tensile yield stress σ_t=2 MPa with linear softening (H=0.65 GPa) The numerical dynamic simulations were performed with the strain rate varying between 10^{-5} 1/s and 10^{1} 1/s. The numerical results with the elasto-visco-plastic model with non-local softening (l_c=5 mm) and different viscosity parameters: τ=1×10^{-6} s, 1×10^{-5} s, 2×10^{-5} s, 1×10^{-4} s and 2×10^{-4} s (simulation #1) were compared with those with the elasto-plastic model with non-local softening (l_c=5 mm) (simulation #2). The number of four-node tetrahedrons was 8007, their size was 5-10 mm [(1-2)×l_c].

Similarly as in compression, the calculated dynamic increase factor is underestimated as compared to both the experiments (Yan and Lin (2006)) and the CEB-FIP Model Code 1990 (1993) with modifications made by Malvar and Ross (1998) for the small strain rates $\dot{\varepsilon}$ <1 1/s) and overestimated for large strain rates ($\dot{\varepsilon} \geq 1$ 1/s) as compared to the CEB-FIP Model Code (Fig. 18). An increase of a viscosity parameter leads to a better accordance with the comparative data for the strain rate $\dot{\varepsilon}$ <1 1/s. In turn, for the higher strain rate ($\dot{\varepsilon} \geq 1$ 1/s), the calculated dynamic effect is quite close to the CEB-FIP Model Code when using a very small viscosity parameter τ (τ =1×10^{-6} s). In analyses without viscosity (simulation #2), the strength does not increase with growing strain rate.

For the small strain rates ($\dot{\varepsilon}$ <10^{-1} 1/s), a localized zone is obtained in the specimen mid-region close to its widening and its width is about 23 mm (Fig. 19). For $\dot{\varepsilon}$ =1 1/s two localized zone are obtained in the specimen mid-region with the similar width of about 21 mm. In turn, for $\dot{\varepsilon}$ =10^{1} 1/s, a localized region occurs close to the specimen top. The experimental results (Fig. 19B) show that for small loading rates, the fracture zone mainly passes through the mortar and aggregate-mortar interfaces which leads to a rough surface (Fig. 19Ba). In turn, for more rapid loading, the fractured surfaces become more flat (cracks also propagate through aggregate) (Figs. 19Bb and 19Bc). The calculated load-displacement curve for $\dot{\varepsilon}$ >1 1/s exhibits a stiffer response in the elastic domain due to inertia effects (Fig. 20). For the small strain rates $\dot{\varepsilon}$ <10^{0} 1/s, the width of localized zones is constant irrespectively of the strain rate and the load-displacement curves are almost identical (similarly as in uniaxial compression). The strain rate effect does not occur for the small strain rates $\dot{\varepsilon}$ <1 1/s using our formulation since elastic viscosity is not taken into account. The strain development is strongly affected by the very high strain rate 10^{1} 1/s only. A diffused localized zone occurs close to the specimen top where the vertical normal strain is prescribed - caused by a stress wave reflection. A similar result was obtained for ceramic materials (Denoual 1998, Ragueneau and Gatuingt 2003), i.e. for the high strain rate, a cracking process was diffuse (without localization) that lead to an strength increase.

The influence of the mesh density on FE results using our elasto-visco-plastic model is demonstrated in Fig. 21. The calculation with τ = 2×10^{-5} s and l_c =10 mm were performed with the different meshes including 482-30469 four-node tetrahedron elements assuming 2 different strain rates: $\dot{\varepsilon}$ =10^{-2} 1/s (Fig. 21(a)) and $\dot{\varepsilon}$ =10^{1} 1/s (Figs. 21(b) and 21(c)). For the smaller strain rate of $\dot{\varepsilon}$ =10^{-2} 1/s, the calculated load-displacement curves are almost the same for all meshes (Fig. 21(a)). However, for the large strain rate, $\dot{\varepsilon}$ =10^{1} 1/s, applied instantaneously at the start of each time step and being constant throughout the time step, the results are solely mesh-independent with the very fine FE meshes including more than 8'000 elements, 5-10 mm large [(0.5-1)×l_c] (Fig. 21(b)). It is due to the difference between a theoretical and numerical wave velocity during impact loads (Bažant 1978, Roth *et al*. 2009). According to Roth *et al*. (2009), 15/16 elements per wavelength are required for accurate FE results during impact loads. The large strain rate ($\dot{\varepsilon}$ =10 1/s) was also applied assuming a smooth polynomial time variation of the displacement during the

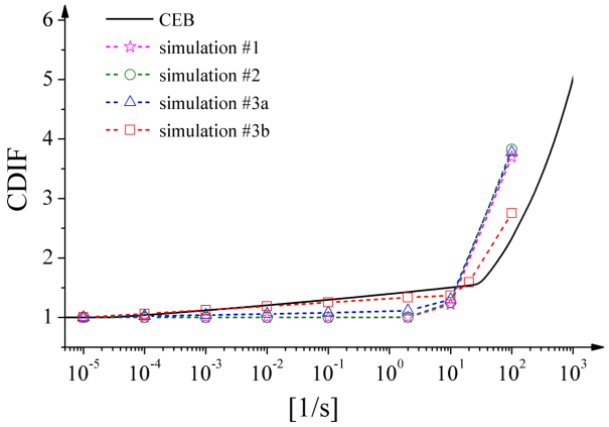

Fig. 15 Calculated CDIF in dynamic 3D FE simulations as compared with CEB curve: elasto-plastic model with non-local softening (simulation #1), elasto-visco-plastic model with non-local softening and relaxation time τ=1×10^{-6} s (simulation #2), elasto-plastic model with non-local softening and stress modifications by Eq. (11) with C_1=1×10^{-6} and C_2=80×10^{-4} (simulation #3a) and stress modifications by Eq. (12) $\dot{\varepsilon}_S$ =10^{-5}, C_1=0.05, C_2=0.02, C_3=0.07 and C_4=-0.002 (simulation #3b)

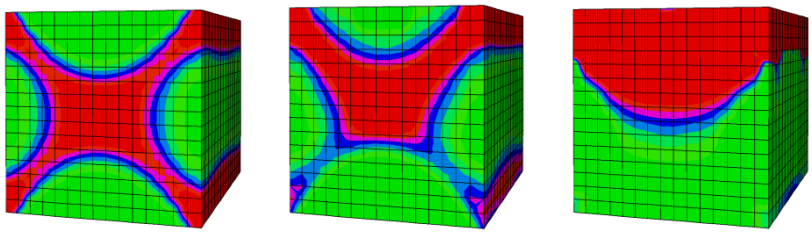

a) b) c)

Fig. 16 The contours of non-local softening parameter from 3D FE dynamic simulations for different prescribed strain rates: a) from 10^{-5} 1/s up to 10^{0} 1/s, b) 10^{1} 1/s and c) 10^{2} 1/s using elasto-plastic model with non-local softening (l_c=5 mm) and stress modification by Eq. (12)

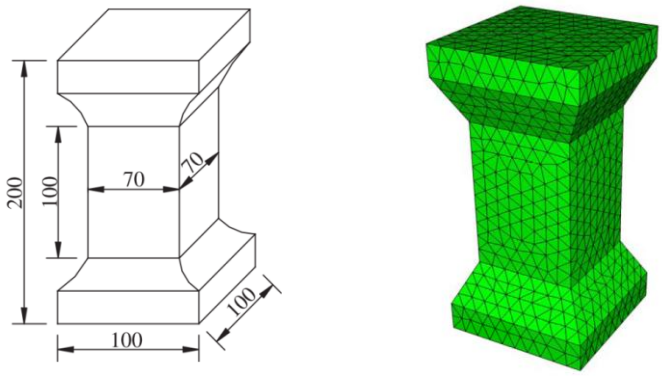

a) b)

Fig. 17 Uniaxial tension with of dumbbell-shaped concrete specimen (Yan and Lin (2006)): geometry (a) and FE mesh (b)

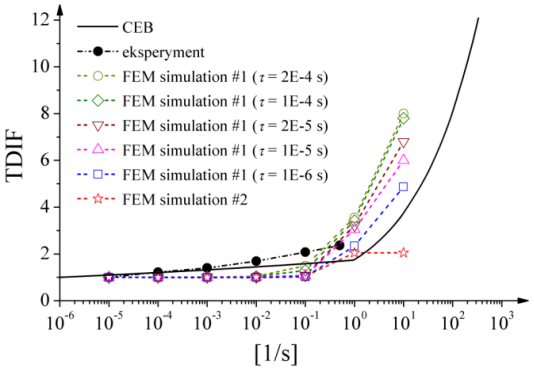

Fig. 18 Dynamic 3D FE results of uniaxial tension as compared to TDIF by CEB for different prescribed strain rates at different relaxation times τ (#1 - elasto-visco-plastic model with non-local softening and #2 - elasto-plastic model with non-local softening)

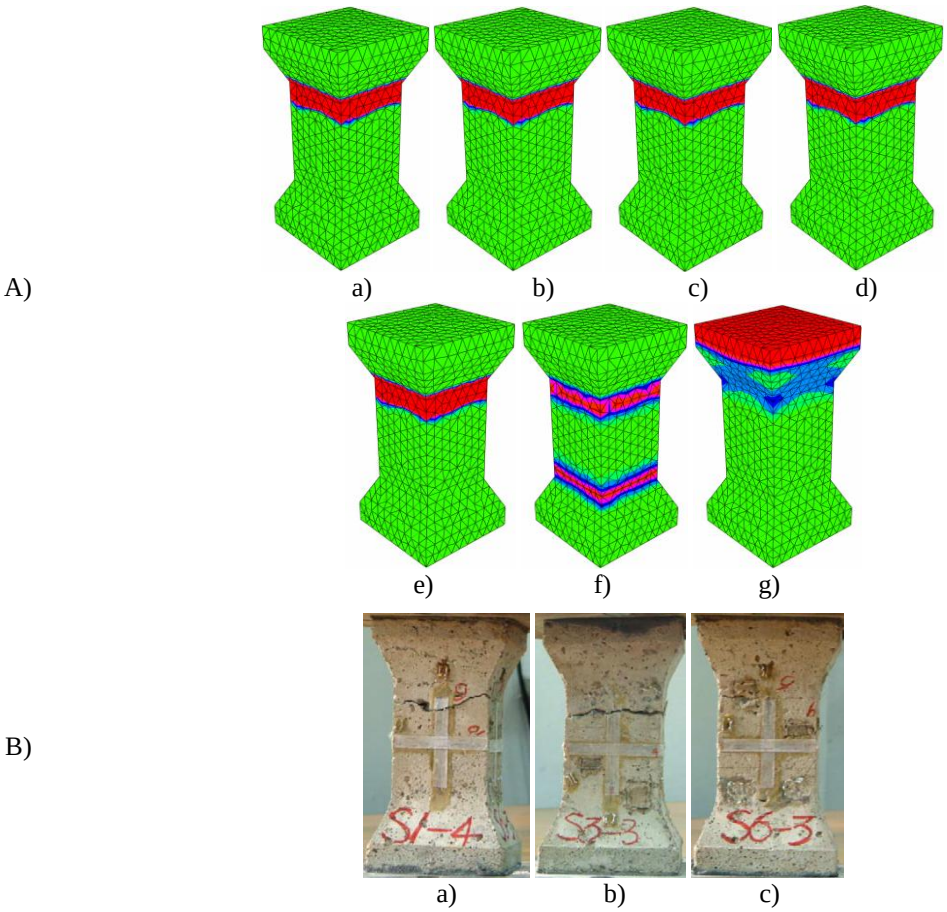

Fig. 19 The contours of non-local softening parameter from 3D FE dynamic simulations (A) at different prescribed strain rates $\dot{\varepsilon}$: a) 10^{-5} 1/s, b) 10^{-4} 1/s, c) 10^{-3} 1/s, d) 10^{-2} 1/s, e) 10^{-1} 1/s, f) 10^{0} 1/s, g) 10^{1} 1/s using elasto-visco-plastic model with non-local softening (l_c=5 mm, τ=1×10^{-6} s) and experimental failure mode Yan and Lin (2006) (B) at $\dot{\varepsilon}$: a) 10^{-5} 1/s, b) 10^{-3} 1/s and c) $10^{-0.3}$ 1/s

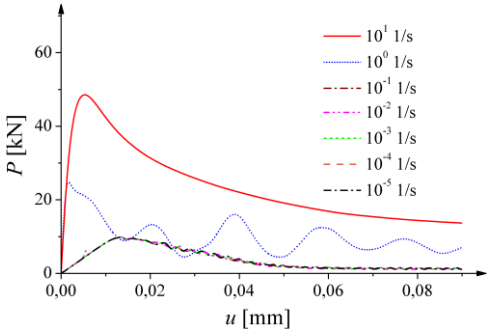

Fig. 20 The load-displacement curves from 3D FE dynamic simulations for different prescribed strain rate $\dot{\varepsilon}$ using elasto-visco-plastic model with non-local softening (l_c=5 mm, τ=1×10^{-6} s)

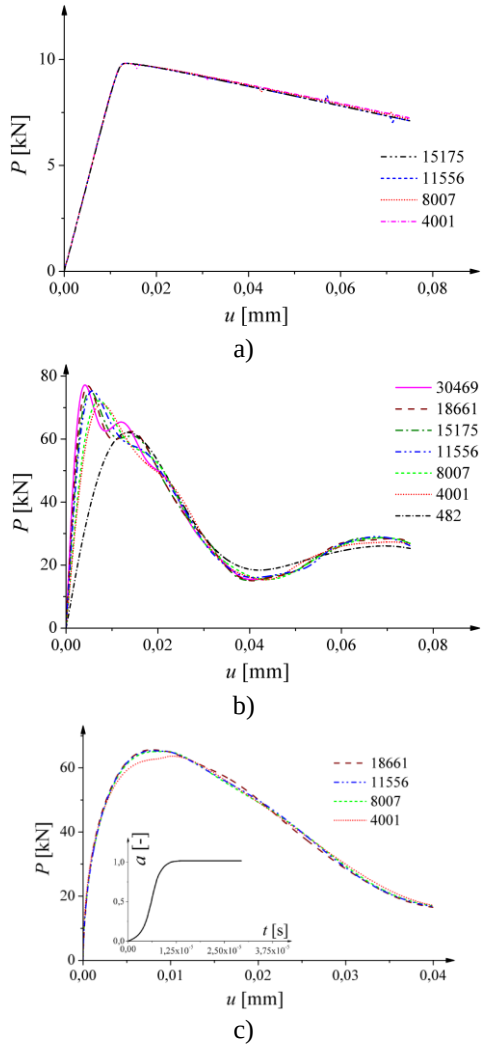

Fig. 21 Influence of 3D mesh density on calculated 3D load-displacement curves at different strain rates: a) $\dot{\varepsilon}$ =10^{-2} 1/s, b) $\dot{\varepsilon}$ =10^{1} 1/s (applied instantaneously) and c) $\dot{\varepsilon}$ =10^{1} 1/s (prescribed smoothly during time *t* in form of polynomial displacement increment factor *a*)

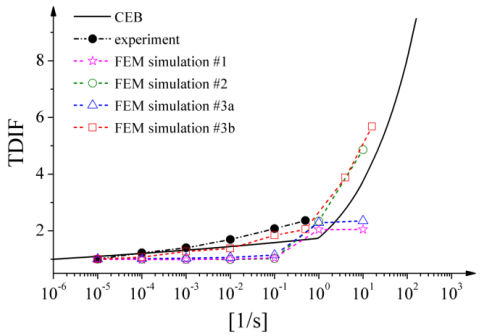

Fig. 22 Dynamic 3D FE simulations of TDIF as compared with CEB curve by considering stress modifications by Eqs.11-12: #1 - elasto-plastic model with non-local softening, #2 - elasto-visco-plastic model with non-local softening (τ=1×10^{-6} s), #3a - elasto-plastic model with non-local softening and stress modifications by Eq. (11) with C_1=1×10^{-6} and C_2=80×10^{-4}, #3b - elasto-plastic model with non-local softening and stress modifications by Eq. (12) with $\dot{\varepsilon}_S$=10^{-5}, C_1=0.05, C_2=0.02, C_3=0.07 and C_4=-0.002

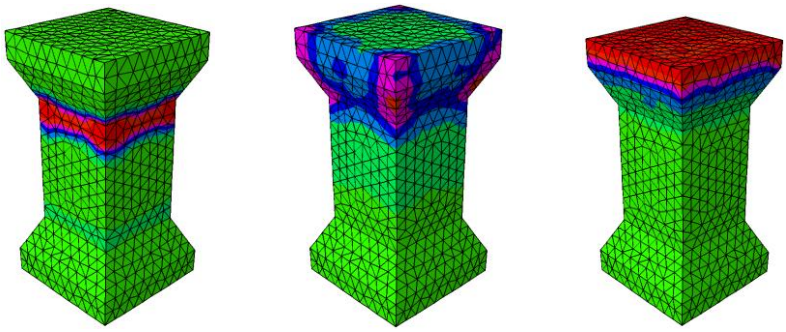

a) b) c)

Fig. 23 The contours of non-local softening parameter from 3D FE dynamic simulations for different prescribed strain rates $\dot{\varepsilon}$: a) from 10^{-5} 1/s to 10^{-1} 1/s, b) 10^{0} 1/s and c) 10^{1} 1/s using elasto-plastic model with non-local softening and stress modification by Eq. (12) (l_c=5 mm)

time of 0.0000125 s (Fig. 21(c)). The results were mesh-independent for the relatively coarse meshes (including less than 8'000 elements), Fig. 21(c).

The use of the elasto-plastic model with the stress modification by Eqs. (11) or (12) leads to the results similar to those of compression (Figs. 22 and 23). The shape of the curves is in agreement with the experimental data and CEB-FIP Model Code in particular for the simulation #3b. For this simulation, the calculated increase factor shows good accordance with the experimental data and CEB-FIP Model Code for $\dot{\varepsilon} \leq 10^{-1}$ 1/s and is overestimated for $\dot{\varepsilon} > 10^{-1}$ 1/s. In the case of the elasto-plastic model with non-local softening and the stress modification by Eq. (12) for the small strain rates ($\dot{\varepsilon} \leq 10^{-1}$ 1/s), similarly as in previous calculation, a localized zone is obtained in the specimen mid-region close to its widening and its width is about 21 mm (Fig. 23). For $\dot{\varepsilon} \geq 1$ 1/s, the shape of strain localization changes – a wide region appears at the specimen upper part.

The results for both uniaxial tension and compression show that the material viscosity (due to free water in a capillary mortar system) was not reflected using our elasto-visco-plastic

formulation. The elasto-plastic model with stress modifications Eq. (12) provided clearly better results for low strain rates but still overestimated results for highest strain rates During compression, the strengthening effect with increasing strain rate was mainly due to inertial forces. The effect of inertial forces during tension was negligible.

4.3 Three-point bending

The numerical results with notched concrete beams 400 mm long under three-point bending were directly compared with the experimental data from Zhang *et al*. (2009). In laboratory tests, two experimental set-ups were used: a hydraulic servo-controlled machine (for low loading velocities 10^{-4}-10^{1} mm/s) and drop-weight impact instrument (for high loading velocities 10^{2}-10^{3} mm/s). The beam cross-section was 100×100 mm^2 (B×D) (Fig. 24). The deformation was induced in FE analyses by imposing always a constant velocity v on one mid-node at the top edge. The plane stress calculations were carried out with the mesh consisting of 3758 triangular elements with the size of 3-5 mm (0.6-1×l_c). When using the Rankine criterion, the FE results are similar for plane stress and strain conditions (Tejchman and Bobiński 2013).

The numerical calculations were carried out using the elasto-visco-plastic model with viscosity ($\tau = 1\times10^{-6}$ s) and the elasto-plastic model with the stress modification given either by Eq. (11) or Eq. (12) (Figs. 25 and 26, respectively). Both models were used in their non-local versions with l_c = 5 mm.

The calculated strength increases with increasing loading velocity. For low loading rates, a satisfactory agreement with respect to the beam strength is achieved between experiments and calculations for the elasto-plastic model with the stress modification given by Eq. (12) (Figs. 25(b) and 26). The calculated softening rate is independent of the loading velocity (for both models) in contrast to experiments where it decreases with increasing loading velocity. The calculated initial stiffness is higher than in experiments for the elasto-visco-plastic model. For high loading velocities, the calculated maximum vertical force is overestimated for both models (Figs. 25(a), 25(b) and 26). No strength increase is obtained for very small loading velocities in elasto-visco-plastic analyses (Fig. 25(a)).

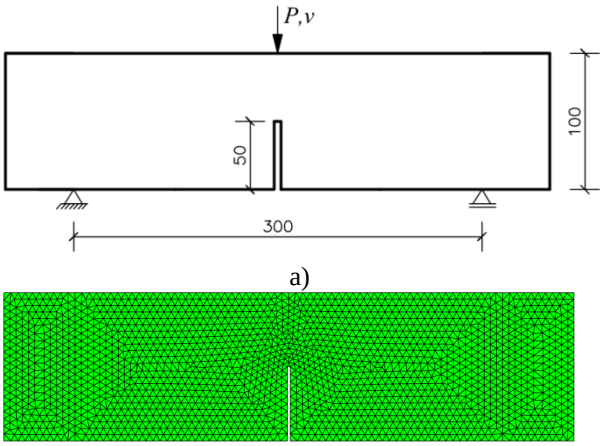

Fig. 24 Geometry (a) and mesh discretization (b) for concrete beams under three-point bending (Zhang *et al*. 2009)

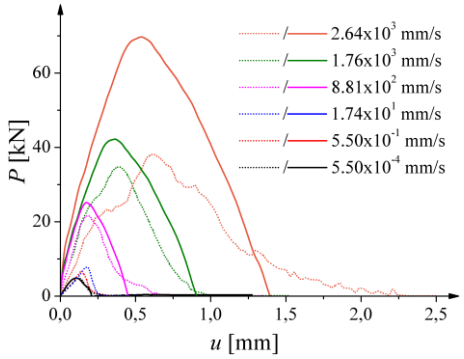

a)

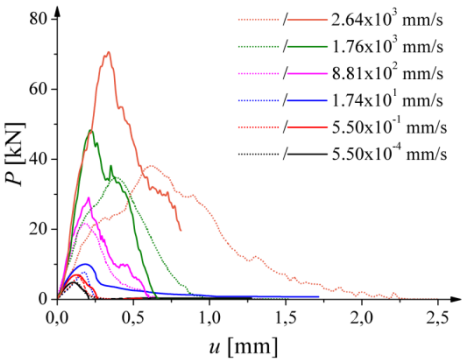

b)

Fig. 25 The load-displacement curves from dynamic FE analyses of three-point bending with different loading velocities v as compared to experiments (Zhang *et al.* 2009) (FEM – solid lines and experiment – dotted lines): a) elasto-visco-plastic model with non-local softening (l_c=5 mm and τ=1×10^{-6} s), b) elasto-plastic model with non-local softening (l_c=5 mm) and stress modification by Eq.12 ($\dot{\varepsilon}_S$ =10^{-5}, C_1=0.05, C_2=0.02, C_3=0.07 and C_4=-0.002)

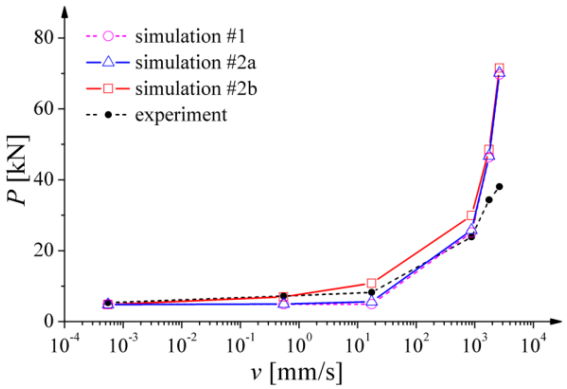

Fig. 26 Relationship between maximum vertical force P and loading velocity v in FE calculations and experiments (Zhang *et al*. 2009): #1 - elasto-visco-plastic model with non-local softening (l_c=5 mm) with viscosity (τ=1×10^{-6} s), #2a - elasto-plastic model with non-local softening (l_c=5 mm) and stress modification by Eq. (11) (C_1=1×10^{-6} and C_2=80×10^{-4}), #2b - elasto-plastic model with non-local softening (l_c=5 mm) and stress modification by Eq. (12) ($\dot{\varepsilon}_S$ =10^{-5}, C_1=0.05, C_2=0.02, C_3=0.07 and C_4 = -0.002)

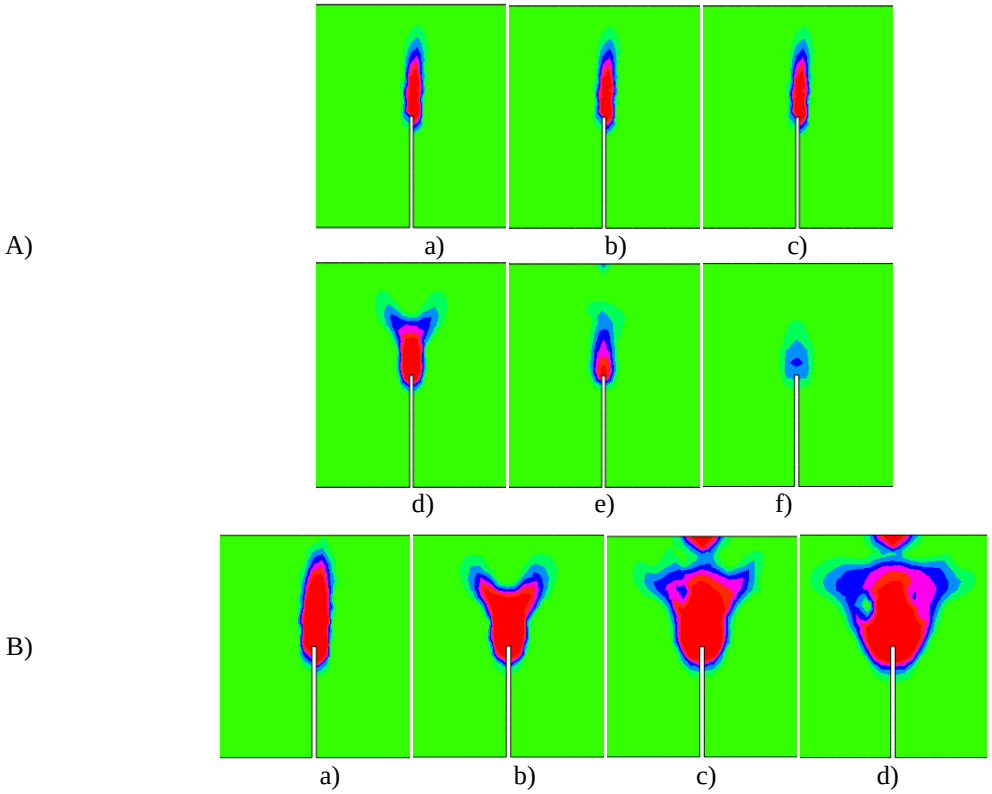

Fig. 27 The contours of non-local softening parameter above the notch from 3D FE dynamic simulations (elasto-visco-plastic model with non-local softening and viscosity (l_c=5 mm, τ=1×10^{-6} s) at different loading velocities: a) 5.5×10^{-4} mm/s, b) 5.5×10^{-1} mm/s, c) 1.74×10^{1} mm/s, d) 8.81×10^{2} mm/s, e) 1.76×10^{3} mm/s, f) 2.64×10^{3} mm/s at vertical displacement u=0.5 mm (A) and u=1 mm (B)

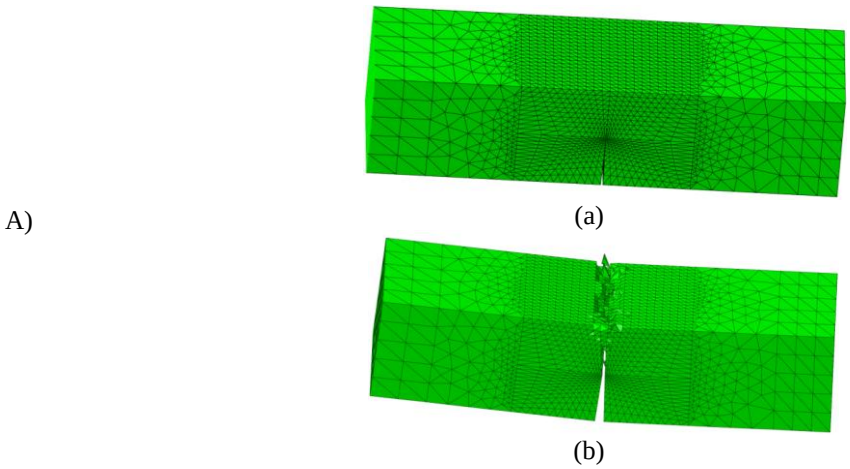

Fig. 28 Dynamic 3D FE analyses of three-point bending with loading velocity v=8.81×10^{2} mm/s and v=2.64×10^{3} mm/s as compared to experiment (Zhang *et al.* 2009) using elasto-visco-plastic model with non-local softening: A) FE mesh (a) initial and b) deformed (v=2.64×10^{3}) and B) load-displacement diagram (a) without stiffness reduction, b) with stiffness reduction, c) experiment)

B)

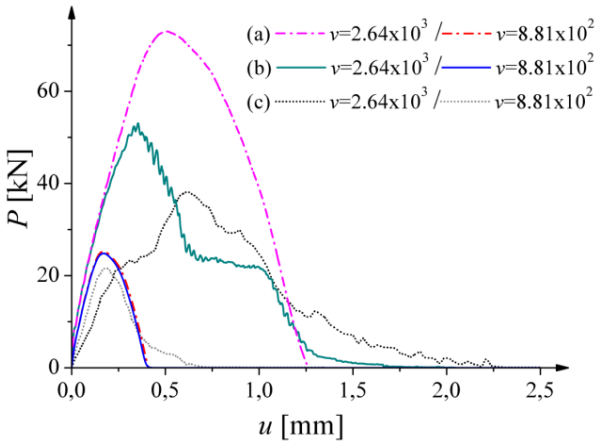

Fig. 28 Continued

For the prescribed loading velocity v from 5.5×10^{-4} mm/s up to 1.74×10^{1} mm/s, a localized zone in the form of a candle flame is numerically obtained with the width of about 17 mm (at u=1 mm) (Fig. 27). In turn for the higher prescribed velocity, a localized zone becomes wider; for v=8.81×10^{2} mm/s two separate zones emerge and for v >1.76×10^{3} mm/s, a localized zone spreads between the notch and top edge.

Finally, to obtain more realistic results for higher loading velocities for concrete, a material stiffness reduction in finite elements (equivalent to a removal of finite elements (Ožbolt *et al.* 2011) was additionally assumed in order to simulate approximately progressive material fragmentation. Such 3D calculations were carried out with the elasto-visco-plastic model (l_c =5 mm and τ =1×10^{-6} s) for the beam of Fig. 24. In each finite element the dissipated energy ($Y = \frac{1}{2}\langle \boldsymbol{\varepsilon}^p \rangle : \langle \boldsymbol{\sigma}^p \rangle$) was calculated wherein the Macauley bracket ($\langle x \rangle = \frac{1}{2}(|x| + x)$) ensured the occurrence of tensile stresses/strains only. This energy was then compared with the softening magnitude (expressed by the area under the softening function during uniaxial tension g_f). If the calculated energy exceeded in one integration point of the finite element the assumed value of g_f (e.g. g_f=3150 N/m^2), both the element stiffness was reduced to a very small value to avoid the singularity of the tangent stiffness operator and the finite element was removed (Fig. 28Ab). The 3D calculations for the intermediate (v = 8.81×10^{2} mm/s) and high loading velocity (v=2.64×10^{3} mm/s) (Zhang *et al.* (2009)) were carried out with the FE mesh consisting of 60486 four-node tetrahedrons within the size range of 1-17 mm [(0.2-3.4)×l_c] (Fig. 28Aa). The smallest elements were assumed close to the notch.

The calculated beam strength with a stiffness reduction (Fig. 28Bb) is obviously significantly smaller as the usual one (Fig. 28Ba) and is closer to the experiment (Fig. 28Bc) in the range of high loading velocities. Due to a sudden reduction of the beam stiffness, stress-strain curves exhibit small oscillations after the peak. In turn for intermediate velocities, the influence of a stiffness reduction is significantly less pronounced. A stochastic distribution of material properties might further improve the numerical results.

5. Conclusions

The FE results for uniaxial compression differed from the CEB recommendations based on the experimental outcomes. The calculated dynamic increase factor using an elasto-visco-plastic model with non-local softening was too small for small strain rates and was too high for high strain rates as compared to CEB and *fib* Model Code recommendations. Thus, viscosity in a plastic domain was not sufficient to accurately capture rate-dependent effects in compression. In particular it had only a minor influence for high strain rates. The evident influence of inertia forces on the results (strength and shape of localized zones) for high strain rates was observed. In the case of an elasto-plastic approach with stress modifications, the improvement in results was observed in particular for small strain rates.

In compression, the overlapping effect of both the non-locality and viscosity occurred but only for fast loading. The width of shear zones increased with increasing strain rate and characteristic length of micro-structure. However, from physical point of view it remains questionable to use a non-local approach for loading rates where failure mechanism is strongly affected by the fragmentation phenomena.

Similarly under tension and bending, the calculated dynamic increase factor using elasto-visco-plastic model was underestimated as compared to both the experiments and CEB-FIP Model Code for the small strain rates and overestimated for large strain rates. Again using elasto-plastic model with stress modifications lead to better agreement with experimental outcomes in particular for small strain rates. The strain localization was affected by very high strain rates only. The dynamic results were mesh-independent for very high strain rates instantaneously prescribed to the specimen if the element size was approximately equal to $1\times l_c$.

Summarizing a strengthening effect was obtained in concrete with increasing strain rates under compression, tension and bending due to the presence of plastic viscosity and inertial forces. Viscosity in a plastic domain might be used to a limited strain rate and loading velocity range for the concrete behaviour description under tension and bending ($\dot{\varepsilon}=10^0$-10^2 1/s, $v=10^1$-10^2 mm/s). In turn under compression, it had a minor influence in contrast to the effect of inertial forces. An improved response of an elasto-visco-plastic model (i.e. better rendering of experimental values of CDIF and TDIF) could be achieved by making the relaxation time τ as a decreasing function of the visco-plastic strain rate $\dot{\gamma}^{vp}$ (i.e. having a large value of the relaxation time for low strain rates and a very small one for high strain rates). In order to propose a specific form of such a function, further numerical research works are needed.

The elasto-plastic model with stress modifications provided realistic results for low strain rates but again overestimated results for high strain rates (more realistic results might be obtained with the more accurate limit values of the second strain rate invariant in Eq. (12)). Considering the additional stiffness reduction to simulate fragmentation significantly improved the numerical results but not sufficiently. Thus, the further research works are needed by taking also into account viscosity in an elastic domain for low strain rates and material fragmentation for high strain rates and by taking a stochastic distribution of material properties.

Acknowledgments

Research work has been carried out within the project: "*Innovative ways and effective methods of safety improvement and durability of buildings and transport infrastructure in the sustainable development*" financed by the European Union (POIG.01.01.02-10-106/09-01). The numerical

calculations were performed on supercomputers of the Academic Computer Centre in Gdańsk TASK.

References

ABAQUS Theory Manual, (2004), Hibbit, Karlsson & Sorensen Inc.

Azevedo, M.N., Lemos, J.V. and de Almeida, J.R. (2008), "Influence of aggregate deformation and contact behavior on discrete particle modeling of fracture of concrete", *Eng. Fract. Mech.*, **75**(6), 1569-1586.

Bažant, Z.P. (1978), "Spurious reflection of elastic waves in non-uniform finite element grids", *Comput. Method. Appl. M.*, **16**, 91-100.

Bažant, Z.P. and Planas, J. (1998), *Fracture and Size Effect in Concrete and Other Quasi-brittle Materials*, CRC Press LLC.

Bažant, Z.P., Caner, F.C., Adley, M.D. and Akers, S.A. (2000), "Fracturing rate effect and creep in microplane model for dynamics", *J. Eng. Mech. ASCE*, **126**, 9, 962-970.

Bažant, Z.P. and Jirásek, M. (2002), "Nonlocal integral formulations of plasticity and damage: survey of progress", *J. Eng. Mech.*, **128**(11), 1119-1149.

Bažant, Z.P. and Caner, F.C. (2013), "Dynamic comminution of quasibrittle solids at high-rate shear under impact and analogy with turbulence", *Proceeding of the Third International Conference on Computational Modeling of Fracture and Failure of Materials and Structures*, *CFRAC 2013*, Prague, Czech Republic, 5–7.06.2013.

Bischoff, P.H. and Perry, S.H. (1991), "Compressive behaviour of concrete at high strain rates", *Mat. Struct.*, **24**, 425-450.

Bischoff, P.H. and Perry, S. H. (1995), "Impact behaviour of plain concrete loaded in uniaxial compression", *J. Eng. Mech. Div ASCE*, **121**, 6.

Bobiński, J. and Tejchman, J. (2004), "Numerical simulations of localization of deformation in quasi brittle materials within non-local softening plasticity", *Comput. Concr.*, **4**, 433-455.

Bobiński, J. and Tejchman, J. (2013), "A coupled continuous and discontinuous approach to concrete elements", *Proc. VIII International Conference on Fracture Mechanics of Concrete and Concrete Structures FraMCoS-8 (eds.: J.G.M. van Mier, G. Ruiz, C. Andrade, R.C. Yu nd X.X. Zhang)*, Toledo, Spain, 11-15.03.2013.

Brara, A. and Klepaczko, J.R. (2006), "Experimental characterization of concrete in dynamic tension", *Mech. Mater.*, **38**, 253-267.

Brinkgreve, R.B. (1994), "Geomaterial models and numerical analysis of softening", Ph.D. Dissertation, Delft University of Technology, Delft.

CEB-FIP Model Code 1990. (1993), Thomas Telford, London.

Cervera, M., Olivier, J. and Manzoli, O. (1996), "A rate-dependent isotropic damage model for the seismic analysis of concrete dams", *Earthq. Eng. Struct. Dyn.*, **25**, 987-101.

de Borst, R. and Sluys, L.J. (1991), "Localization in a cosserat continuum under static and dynamic loading conditions", *Comput.Method. Appl. M.*, **90**, 1-3, 805-827.

Denoual C. (1998), "Approche probabiliste du comportement l'impact du carbure de silicium: application aux blindages moyens", Ph.D. Dissertation, ENS de Cachan.

Denoual, C. and Hild, F. (2000), "A damage model for the dynamic fragmentation of brittle solids", *Comp. Meth. Apll. Mech. Eng.*, **183**, 247-258.

Duvaut, G. and Lions, J.L. (1972), *Les Inequations en Mecanique et en Physique*, Dunod, Paris.

Drucker, D.C. and Prager, W. (1952), "Soil mechanics and plasticity analysis of limit design", *Quart. J. Appl. Math.*, **10**, 157–162.

Eibl, J. and Schmidt-Hurtienne, B. (1999), "Strain-rate-sensitive constitutive law for concrete", *J. Eng. Mech.*, **125**, 1411-1420.

Ferrara, I. and di Prisco, M. (2001), "Mode I fracture behaviour in concrete: nonlocal damage modelling",

ASCE J. Eng. Mech., **127**(7), 678-692.
fib. Model Code 2010 (2012), Final draft, fib Bulletin 65.
Gary, G. (1990), *Essais à Grande Vitesse sur Béton. Problèmes Spécifiques*, Scientifique Rapport GRECO (edité par J. M. Reynouard).
Gatuingt, F. and Pijaudier-Cabot, G. (2002), "Coupled damage and plasticity modelling in transient dynamic analysis of concrete", *Int. J. Numer. Anal. Meth. Geomech.*, **26**, 1-24.
Georgin, J.F. and Reynouard, J.M. (2003), "Modelling of structures subjected to impact: concrete behaviour under high strain rate", *Cement Concrete Compos.*, **25**, 131-143.
Grady, D. (2008), "Fragment size distributions from the dynamic fragmentation of brittle solids", *Int. J. Imp. Eng.*, **35**, 1557-1562.
Häußler-Combe, U. and Kühn, T. (2012a), "Failure modelling of concrete with a novel strain rate sensitive viscoelastic retarded damage material formulation", *European Congress on Computational Methods in Applied Sciences and Engineering (ECCOMAS 2012), J. Eberhardsteiner et.al. (eds.)*, Vienna, Austria, 2012.
Häußler-Combe, U. and Kühn, T. (2012b), "Modeling of strain rate effects for concrete with viscoelasticity and retarded damage", *Int. J. Impact. Eng.*, **50**, 17-28.
Hentz, S., Daudeville, L. and Donze, F. (2004), "Identification and validation of a discrete element model for concrete", *J. Eng. Mech.*, **130**(6), 709-719.
Hughes, T.J.R. and Winget, J. (1980), "Finite rotation effects in numerical integration of rate constitutive equations arising in large deformation analysis", *Int. J. Numer. M. Eng.*, **15**, 1862-1867.
Jankowiak, T. (2009), "Failure criteria under quasi-static and dynamic loads", Ph.D. Dissertation, Poznań University of Technology, Poznań.
Jankowiak, T., Rusinek, A. and Lodygowski, T. (2011). "Validation of the klepaczko-malinowski model for friction correction and recommendations on split hopkinson pressure bar", *Finite Elem. Anal. Des.*, **47**(10), 1191-1208.
Jirásek, M., and Rolshoven, S. (2006), "Comparison of integral-type nonlocal plasticity models for strain-softening materials", *Int. J. Eng. Sci.*, **41**, 13-14, 1553-1602.
Lee, J., and Fenves, G.L. (1998), "Plastic-damage model for cyclic loading of concrete structures", *J. Eng. Mech.*, **124**(8), 892-900.
Majewski, T., Bobinski, J. and Tejchman, J. (2008), "FE-analysis of failure behaviour of reinforced concrete columns under eccentric compression", *Eng. Struct.*, **30**(2), 300-317.
Malvar, L. J. and Ross, C.A. (1998), "Review of strain rate effects for concrete in tension", *ACI Mater. J.*, **95**, 735-739.
Marzec, I., Bobiński, J. and Tejchman, J. (2007), "Simulations of crack spacing in reinforced concrete beams using elastic-plasticity and damage with non-local softening", *Comput. Concr.*, **4**(5), 377-403.
Menetrey, P. and Willam, K.J. (1995), "Triaxial failure criterion for concrete and its generalization", *ACI Struct. J.*, **92**(3), 311-318.
Moonen, P., Carmeliet, J. and Sluys, L.J. (2008), "A continuous-discontinuous approach to simulate fracture processes", *Philos. Mag.*, **88**, 3281-3298.
Nagtegaal, J. C., Parks, D. M. and Rice J. R. (1977), "On numerically accurate finite element solutions in the fully plastic range", *Comput. Method. Appl. M.*, **4**, 153-177.
Nemes, J.A. and Speciel, E. (1996), "Use of a rate-dependent continuum damage model to describe strain-softening in laminated composites", *Comput. Struct.*, **58**, 1083-1092.
Ortiz, M. and Simo, I.C. (1986), "An analysis of a new class of integration algorithms for elastoplastic constitutive relation", *Int. I. Num. Method. Eng.*, **23**, 353-366.
Ožbolt, J. and Reinhardt, H.W. (2005), "Rate dependent fracture of notched plain concrete beams", *Proceedings of the 7th international conference CONCREEP-7, (ed. by Pijaudier Cabot, Gerard & Acker)*, 57-62.
Ožbolt, J., Sharma, A. and Reinhardt, H-W. (2011), "Dynamic fracture of concrete compact tension specimen", *Int. J. Solid. Struct.*, **48**(10), 1534-1543.
Pająk, M. (2011), "The influence of the strain rate on the strength of concrete taking into account the

experimental techniques", *Architect. Civ. Eng.-Environ. J. (ACEE)*, **3**, 77-86.
Pedersen, R.R., Simone, A. and Sluys, L.J. (2008), "An analysis of dynamic fracture in concrete with continuum visco-elastic visco-plastic damage model", *Eng. Fract. Mech.*, **75**, 3782-3805.
Pedersen, R.R. (2009), "Computational modelling of dynamic failure of cementitious materials", Ph.D. Dissertation, TU Delft, Delft.
Perzyna, P. (1966), "Fundamental problems in viscoplasticity", *Adv. Appl. Mech., Academic Press*, **9**, 243-377.
Pijaudier-Cabot, G. and G., Bažant, Z.P. (1987), "Nonlocal damage theory", *ASCE J. Eng. Mech.*, **113**, 1512-1533.
Pijaudier-Cabot, G., Haidar, K. and Dube, J.F. (2004), "Non-local damage model with evolving internal length", *Int. J. Numer. Anal. M.*, **28**, 633-652.
Polizzotto, C., Borino, G. and Fuschi, P. (1998), "A thermodynamic consistent formulation of nonlocal and gradient plasticity", *Mech. Res. Communic.*, **25**, 75-82.
Ragueneau, F. and Gatuingt, F. (2003), "Inelastic behaviour modelling of concrete in low and high strain rate dynamics", *Comput. Struct.*, **81**, 1287-1299.
Rankine, W.J.M. (1858), *A Manual of Applied Mechanics*, London and Glasgow: Richard Griffin and Company, Publishers to the University of Glasgow.
Rossi, P. (1991), "A physical phenomenon which can explain the mechanical behaviour of concrete under high strain rates", *Mater. Struct.*, **24**, 422-424.
Roth, S., Oudry, J., El-Rich, M. and Shakourzadeh, H. (2009), "Influence of mesh density on a finite element model's response under dynamic loading", *J. Biol. Phys. Chem.*, **9**, 210-219.
Rousseau, J., Frangin, E., Marin, P. and Daudeville, L. (2009), "Multidomain finite and discrete elements method for impact analysis of a concrete structure", *Eng. Struct.*, **31**(11), 2735-2743.
Sercombe, J., Ulm, F.J. and Mang, H.A. (2000), "Consistent return mapping algorithm for chemoplastic constitutive laws with internal couplings", *Int. J. Numer. Meth. Eng.*, **47**, 75-100.
Simone, A. (2003), "Continuous-discontinuous modelling of failure", Ph.D. Dissertation, TU Delft, Delft.
Skarżyński, L. and Tejchman, J. (2010), "Calculations of fracture process zones on meso-scale in notched concrete beams subjected to three-point bending", *European J. Mech. A Solid*, **29**, 746-760.
Skarżyński, L., Syroka, E. and Tejchman, J. (2011), "Measurements and calculations of the width of the fracture process zones on the surface of notched concrete beams", *Strain*, **47**, e319-e332.
Sluys, L.J. and de Borst R. (1992), "Wave propagation and localization in a rate-dependent cracked medium-model formulation and one-dimensional examples", *Int. J. Solid Struct.*, **29**, 2945-58.
Strömberg, L. and Ristinmaa, M. (1996), "FE-formulation of nonlocal plasticity theory", *Comput. Method. Appl. M.*, **136**, 127-144.
Suaris, W. and Shah, S.P. (1984), "Rate-sensitive damage theory for brittle materials", *J. Eng. Mech.*, **110**, 985-997.
Syroka, E., Tejchman, J. and Mróz, Z. (2013), "FE calculations of a deterministic and statistical size effect in concrete under bending within stochastic elasto-plasticity and non-local softening", *Eng. Struct.*, **48**, 205-219.
Syroka-Korol, E. and Tejchman, J. (2013), "Experimental investigations of size effect in reinforced concrete beams failing by shear", *Eng. Struct.*, http://dx.doi.org/10.1016/j.engstruct.2013.10.012.
Tejchman, J. and Bobiński, J. (2013), *Continuous and Discontinuous Modelling of Fracture in Concrete Using FEM*, Springer, Berlin-Heidelberg, Germany.
Vermeer, P.A. and Brinkgreve, R.B.J. (1994), "A new effective non-local strain-measure for softening plasticity", *Localisation and Bifurcation Theory for Soils and Rocks (edited by: Chambon, R., Desrues, J. and Vardoulakis, I.)*, Balkema, 89-100.
Wang, W.M., Sluys, L.J. and de Borst, R. (1997), "Viscoplasticity for instabilities due to strain softening and strain-rate softening", *Int. J. Numer. Meth. Eng.*, **40**, 3839-64.
Werner, S. and Thienel, K.-Ch. (2011), "Influence of impact velocity on the fragment formation of concrete specimens", *Int. Conference Particles*, 211-221, Barcelona.
Winnicki, A. (2007), "Viscoplastic and internal discontinuity models in analysis of structural concrete",

Habilitation Monograph, Cracow University of Technology, Cracow.
Winnicki, A., Pearce, C.J., Bićanić, N. (2001), "Viscoplastic Hoffman consistency model for concrete", *Comput. Struct.*, **79**, 7-19.
Zheng, D. and Li, Q. (2004), "An explanation for rate effect of concrete strength based on fracture toughness including free water viscosity", *Eng. Fract. Mech.*, **71**, 2319-2327.
Zhang, X.X., Ruiz, G., Yu, G.R.C. and Tarifa, M. (2009), "Fracture behaviour of high strength concrete at a wide range of loading rates", *Int. J. Impact. Eng.*, **36**, 1204-1209.
Yan, D. and Lin, G. (2006), "Dynamic properties of concrete in direct tension", *Cement Concrete Res.*, **36**, 1371-1378.

CC